Research Updates

Development of semiconducting ScN

Bidesh Biswas[1] and Bivas Saha[1,2,3,*]

[1]*International Centre for Materials Science, Jawaharlal Nehru Centre for Advanced Scientific Research, Jakkur, Bangalore 560064, India*
[2]*Chemistry and Physics of Materials Unit, Jawaharlal Nehru Centre for Advanced Scientific Research, Jakkur, Bangalore 560064, India*
[3]*School of Advanced Materials, Jawaharlal Nehru Centre for Advanced Scientific Research, Jakkur, Bangalore 560064, India*

(Received 28 August 2018; revised manuscript received 28 November 2018; published 14 February 2019)

Since the 1960s advances in electronic and optoelectronic device technologies have been primarily orchestrated by III-V semiconductors, which have led to an age of consumer electronic devices with unprecedented social and economic impacts. Group III-V semiconductors such as GaAs, GaN, InAs, and GaP and their solid solution alloys are not only the building blocks of modern solid-state lighting, photodetectors, sensors, and high-speed power-electronic and optoelectronic devices, they have also been actively researched and developed for over six decades to understand and innovate fundamental materials science, physics, and device engineering properties. Yet there is a widespread realization today that contemporary grand challenges of our society such as energy efficient electronics and computing, secure information processing, energy security, imaging, sensing, etc., require more advanced materials and better device integration technologies. At the same time, several important device technologies of the modern era such as thermoelectricity that converts waste heat into electrical energy, plasmonic materials, and devices that could be utilized to harvest optical energy in solar photovoltaics, solar thermophotovoltaics, photocatalysis, etc., also require materials and heterostructure metamaterials that are not possible to achieve with traditional III-V semiconductors. Scandium nitride (ScN) is a group 3 rocksalt nitride semiconductor, which can overcome some of the limitations of traditional III-V semiconductors, and could lead to novel device functionalities. However, unlike other well-known III-V semiconductors, very little attention has been devoted to understand and engineer ScN's physical properties until very recently. In this research update, we detail the progress that has taken place over the last several years to overcome the materials engineering challenges for high-quality epitaxial ScN thin-film growth, analysis of its physical properties, and epitaxial integration of ScN with other rocksalt metallic nitrides. Along with the attractive physical properties common to most transition-metal nitrides such as high hardness, large melting temperature, and chemical, thermal, and morphological stability, ScN also exhibits rocksalt crystal structure with octahedral bonding coordination, indirect band gap, preferential *n*-type and *p*-type doping, and the ability to epitaxially integrate with other metallic materials (such as TiN, ZrN, HfN, etc.) to deposit single-crystalline epitaxial metal/semiconductor multilayers and superlattices without the presence of extended defects. All of these advances could lead to ScN based materials and devices with improved efficiencies and industrial applications.

DOI: 10.1103/PhysRevMaterials.3.020301

I. INTRODUCTION

Advances in electronic and optoelectronic device technologies for over six decades have been primarily orchestrated by semiconductors, which has led to the proliferation of the information technology age with unprecedented social and economic impacts [1,2]. While the silicon based integrated circuit [3–9] is at the heart of this technological revolution, III-V semiconductors have fundamentally transformed consumer electronics, solid-state lighting, high-speed electronics, power-electronic devices, and digital communication industries [10–16]. The III-V semiconductors and their solid solution alloys (such as GaN, InGaN, GaAs, InGaAs, GaP, etc.) have also led to the discovery of many novel scientific concepts such as fractional quantum Hall effect, quantum well lasers, quantum cascade lasers, electron and photon confinements [17–23], etc., and are at the forefront for the exploration of the fundamental physics based concepts in materials science and devices engineering, such as quantum computing, quantum information processing technologies, etc. [24,25]. While all of these advances and continuing improvements of III-V semiconductor based device technologies have helped scientific and societal progress, there is a widespread realization in the III-V materials and device communities today that some of the most important and pressing challenges of our society such as energy security, clean environment, secure information processing, imaging, and sensing require more advanced materials, new device physics concepts, and efficient heterogeneous integration techniques that are currently difficult or impossible to achieve with existing materials.

In comparison to the III-V semiconductors, group 3 [containing scandium (Sc), yttrium (Y), and all the lanthanides and actinides] semiconducting materials have received very little attention historically ("III-V semiconductor" nomenclature in this paper is used to refer to traditional semiconductors

*Corresponding author: bsaha@jncasr.ac.in; bivas.mat@gmail.com

belonging to group 13–15, according to the new IUPAC notation, which were previously referred to as III (A)-V semiconductors in the old IUPAC convention. Similarly the III (B) elements in the old IUPAC notations are referred to as group 3 elements following the new convention in this paper). However, among the group 3 semiconductors, group 3-nitrides have generated great interests in recent years for a variety of applications [26,27]. Scandium nitride (ScN) is a well-known group 3-nitride semiconductor, and could overcome some of the limitations of traditional III-V semiconductors. Along with its heterostructures, ScN could also offer potential solutions in many branches of modern science and engineering. For example, unlike the direct band-gap wurtzite III-nitride semiconductors (such as AlN, GaN, and InN) or zinc-blende arsenide semiconductors (such as GaAs and AlAs), ScN crystallizes in rocksalt [28–31] (cubic) structure and exhibits an indirect band gap of ∼0.9 eV and a direct band gap of 2.2 eV [31–36]. Due to its rocksalt crystal structure, ScN possess octahedral bonding coordination, which is markedly different from tetrahedral coordinated wurtzite III-nitride semiconductors. Such basic differences in the crystal structure, bonding coordination, and electronic structure lead to fundamentally different and interesting properties in ScN that are not common with other semiconductors.

Early interest in ScN research can be dated back to late the 1920s, when Meissner and Franz [37] studied its superconducting properties, and to the 1960s, when several researchers reported on its basic physical properties, such as specific heat, optical absorption, etc. [38–42]. However, poor crystalline quality, lack of understanding about its electronic structure, and unsuccessful attempts to produce preferential *n*-type and *p*-type doping severely limited progress in ScN research and development for a long time. The situation has changed significantly over the last 15–20 years as several researchers have reported on the growth of epitaxial ScN films by a variety of high-vacuum deposition techniques and reported on its physical properties.

ScN has attracted significant interest for its potential applications in thermoelectricity [43–47], as a semiconducting material in epitaxial single-crystalline metal/semiconductor superlattices for their thermoelectric, plasmonic, and thermophotonic applications [48], and for several other solid-state device applications such as substrates for high-quality GaN based devices, as well as for reducing threading dislocation densities in GaN epilayers [49–55]. Like most other transition-metal nitrides (TMNs), ScN is structurally and chemically stable, mechanically hard (23 GPa), and corrosion resistant and possesses an extremely high melting temperature in excess of 2600 °C [39,56]. Due to its rocksalt (cubic) crystal structure, ScN also offers a materials platform for engineering the band structure of alloys with III-nitride semiconductors (AlN, GaN, and InN) for applications where integration of the semiconductor with cubic (rocksalt) metals is required [57]. ScN and its rocksalt solid solution $Al_xSc_{1-x}N$ have been developed and utilized in recent years to deposit epitaxial metal/semiconductor (Hf,Zr)N/ScN multilayers and TiN/(Al,Sc)N superlattices [58–61]. Wurtzite $Al_xSc_{1-x}N$ thin-film alloys have also attracted interest for their large piezoelectric response [62–67], and are actively researched for both bulk and surface acoustic devices. The high melting temperature (>2600 °C) of ScN is also suitable for refractory electronic applications, and for component materials for refractory plasmonic devices. In short, ScN is an emerging nitride semiconductor for future applications and deserves attention to harness its potential for practical devices.

While significant challenges related to ScN based device fabrications and characterizations remain an open scientific and engineering research direction, there is no doubt that the past 15–20 years of research and continuing developments have provided an ideal platform for the exploration of its industrial applications. In this research update article, we outline and discuss the important aspects of ScN research and development, providing a comprehensive description of growth, characterization, and physical properties. We also highlight several ongoing challenges and future research directions on ScN.

II. HISTORICAL PERSPECTIVE

The description of the early history of ScN research and development would not be complete without an explicit reference to the rich history of the discovery of scandium (Sc) metal. During the development of the periodic table of elements in 1869, Mendeleev predicted the existence of "eka-boron" along with the prediction of three other elements lighter than rare-earth elements, gallium as "eka-aluminium," technetium as "eka-manganese," and germanium as "eka-silicon" [68,69]. Nilson, at Uppsala University, Sweden, discovered eka-boron in 1879 and gave it the name "scandium" in honor of Scandinavia, where the mineral containing the element was originally discovered [70,71]. Despite this early discovery, research in scandium and its derivatives remained scarce for the next two to four decades, and was limited to its metallurgical aspects.

In one of the earliest reports, Meissner and Franz [37] studied the superconducting properties of ScN along with several other carbides and nitrides, and found that ScN does not exhibit superconducting properties down to 1.4-K temperature. Detailed analysis of ScN's physical properties, however, started mostly in the early 1960s (see Fig. 1) when Gschneider, Jr. [56] and Samsonov *et al.* [39] reported on its melting temperature, free energy, and enthalpy of formation. The Debye temperature and heat capacity were also calculated and measured during the same time period by Kaufman [42] and Shakhanova *et al.* [41], respectively.

An important milestone in ScN research came about in the early 1970s when Dismukes *et al.* [72,73] deposited ScN thin films using a hybrid vapor phase epitaxy (HVPE) method. Scandium halides were made to react with ammonia in the temperature ranges between 750 and 1150 °C that resulted in ScN thin films on sapphire substrates. Epitaxial thin films deposited with the HVPE method resulted in highly conductive *n*-type films having a carrier concentration 10^{20}–10^{21} cm^{-3}. Dismukes [72] also measured the room-temperature electrical resistivity of 0.4 mΩ cm, which was higher than previous reports. The optical band gap was determined to be 2.1 eV, which was again higher than the previously measured reports of 1.75 eV [74].

In spite of such promising developments in the 1960s and in the early 1970s, research on ScN stagnated for

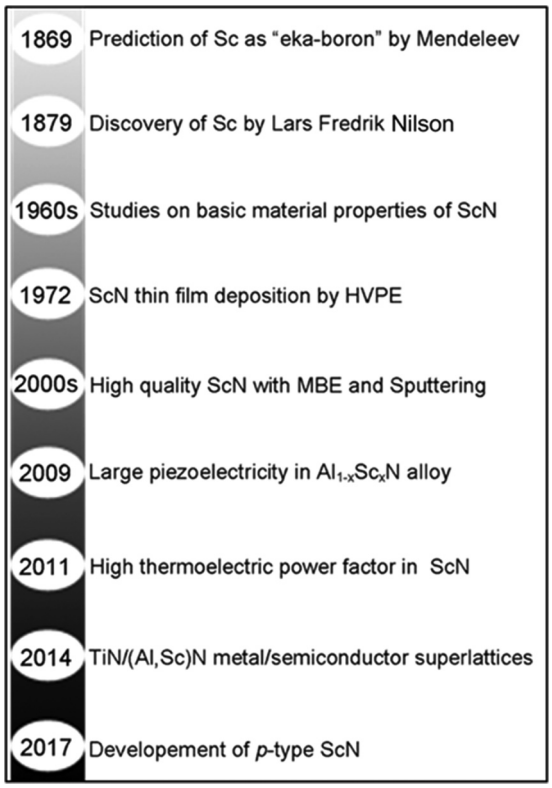

FIG. 1. Historic timeline of important progress in ScN research. The image shows that even though ScN research started long ago much of the important progress was achieved in the last 15–20 years.

the next 25–30 years primarily due to (a) controversy and concerns about its stoichiometry, with some reports questioning whether ScN is inherently nonstoichiometric, which results in self-compensation and defect generation leading to heavy *n*-type doping; (b) controversy about the true nature of its electronic structure (while absorption studies had showed ScN to be a semiconductor, modeling reports indicated ScN to be a semimetal; room-temperature electrical conductivity of ScN was much higher in comparison to traditional semiconductors and approached almost to that of a good metal); and (c) unsuccessful attempts to reduce the *n*-type carrier concentrations, and develop *p*-type ScN, thereby limiting its horizon for device technologies.

The controversy over the stoichiometry was resolved partially in 1985 when x-ray photoelectron spectroscopy (XPS) analysis by Porte [75] demonstrated that ScN is inherently a stoichiometric compound and that, in special situations when the nitrogen to scandium ratio is less than 1, the films correspond to two phase regions, a stoichiometric ScN and another phase of metallic scandium. XPS analysis also indicated the presence of 0.5% nitrogen vacancy that could result in 10^{20}–10^{21} cm^{-3} carriers, and would move the Fermi energy from inside the band gap to the bottom of the conduction band.

The breakthrough in ScN research came about in the late 1990s and in the early 2000s when several groups reported on the growth of high-quality ScN thin films and studied their physical properties.

(a) Gall *et al.* [76–78] employed ultrahigh-vacuum (UHV) reactive magnetron sputtering to deposit epitaxial ScN on (001) MgO substrates that resulted in (001) and (111) oriented film growths. Spectroscopic characterization and density functional theory (DFT) based calculations [35,78] indicated that ScN is an indirect band-gap semiconductor.

(b) Bai and Kordesch [36] successfully deposited ScN using plasma assisted physical vapor deposition (PA-PVD) and reactive rf-sputtering techniques on a range of substrates. The direct band gap was measured to be 2.26 eV, close to the previous reports of Dismukes [72] The results of Kordesch and coworkers [36,79] also showed rectifying behavior of ScN/GaN heterojunctions fabricated with PA-PVD ScN, and metal organic chemical vapor deposited (MOCVD) GaN.

(c) Smith *et al.* [80] deposited smooth ScN thin films using rf molecular-beam epitaxy (MBE). Characterization by x-ray diffraction (XRD), reflection high-energy electron diffraction, scanning tunneling microscopy (STM), and atomic force microscopy (AFM) analysis showed that the Sc to N flux ratio has an important role in the microstructure and stoichiometry of the films. While nitrogen rich conditions resulted in smooth and stoichiometric films, Sc rich conditions resulted in smooth but substoichiometric surfaces.

(d) Moram and coworkers [53,81] used ScN as interlayers and demonstrated threading dislocation density reduction in GaN films by more than two orders of magnitude.

Recent interests in ScN research were catalyzed in the early 2010s, when Kerdsongpanya *et al.* [82] and Burmistrova *et al.* [83] utilized dc-magnetron sputtering techniques to deposit epitaxial ScN thin films, and demonstrated high thermoelectric power factors for thermoelectric applications. Saha *et al.* [84,85] developed epitaxial single-crystalline metal/semiconductor (Hf,Zr)N/ScN multilayers and TiN/(Al,Sc)N superlattices. Hole doped *p*-type ScN thin film was also demonstrated by the incorporation of Mg_xN_y and Mn_xN_y, inside the ScN matrix by Saha *et al.* [33,86]. The *p*-type $Sc_{1-x}Mg_xN$ alloy films also demonstrated [87] high thermoelectric power factors, and enabled the potential of device fabrications.

III. THIN-FILM DEPOSITION AND STRUCTURAL PROPERTIES

A variety of deposition techniques have been utilized over the years for ScN growth such as arc melting of Sc in nitrogen environment [88,89], reaction of scandium halide with ammonia [90–92], reactive magnetron sputtering, evaporation, chemical vapor deposition using halide as reacting agents [93–96], sublimation-recondensation method in a resistively heated tungsten furnace [97,98], MBE [99–101], etc. In this article, we will focus mostly on HVPE, MBE, and reactive magnetron sputtering techniques for high-quality ScN thin-film growth.

A. Hybrid vapor phase epitaxy

Dismukes [72] deposited ScN thin films having a thickness of ~2–3 μm by HVPE method on *c*-plane (0001) and *r*-plane (1102) sapphire substrates. Crystal orientation, crystallinity, and electronic properties of the films were found to depend strongly on the growth temperatures, and an N/Sc ratio of 0.99 ± 0.01 was determined by wet chemistry methods.

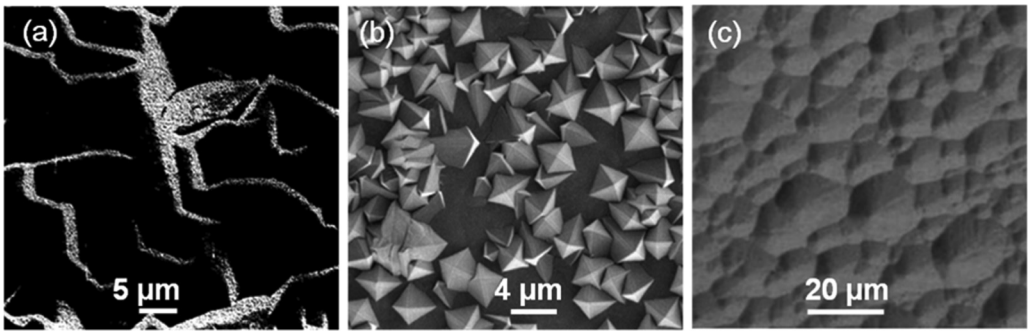

FIG. 2. (a) SEM image of a HVPE deposited single-crystalline (321) ScN surface exhibiting an island-type structure on Al_2O_3 substrates. (b) SEM image of a ScN surface deposited with a substrate temperature of 800 °C and a source temperature of 1000 °C on 6H-SiC substrate. (c) Nomarski microscope surface image of a ScN (001) film with an approximate thickness of 40 μm. Reproduced with permission from Refs. [72,92,102].

At high substrate temperature between 850 and 930 °C, good quality ScN thin films having high electron mobility of 176 $cm^2/V\,s$ and electron concentration as low as $1.9 \times 10^{20}\,cm^{-3}$ were achieved. Deposition temperature beyond 930 °C resulted in polycrystalline film growth. For a typical single-crystalline sample deposited on $\langle 1\bar{1}02\rangle\,\alpha$-$Al_2O_3$ substrate, scanning electron microscopy (SEM) showed an island-type structure [see Fig. 2(a)] having an orientation relationship of $\langle 321\rangle \| \langle 1\bar{1}02\rangle \alpha$-$Al_2O_3$. For different growth conditions, other orientations such as $\langle 100\rangle \| \langle 1\bar{1}02\rangle \alpha$-$Al_2O_3$ and $\langle 111\rangle \| \langle 1\bar{1}02\rangle \alpha$-$Al_2O_3$ were also achieved. HVPE deposited ScN films, however, contained chlorine (Cl) and oxygen (O) impurities in high concentrations, i.e., $[Cl] = 1.8 \times 10^{20}\,cm^{-3}$ and $[O] = 4.4 \times 10^{19}\,cm^{-3}$, respectively, which explained their high *n*-type carrier concentrations.

HVPE method was also employed to deposit ScN thin films on 6H-SiC (0001) substrates. Edgar *et al.* [92] reported epitaxial ScN thin-film growth with (111) orientations at substrate temperatures of 800–900 °C [see Fig. 2(b)]. At higher growth temperature, mixed phase polycrystalline samples with (100) and (111) orientations were achieved. However, the films contained aluminum and chlorine impurities in significantly higher concentrations. The reaction between scandium chloride (reactant) and an alumina tube used to contain Sc metal in the HVPE reactor was assumed to be the source of the aluminum impurities. For thin films deposited at 1000 °C, aluminum concentration was as high as 1.5 at. %, and reduction of the deposition temperature to 800 °C resulted in only slight reduction of Al concentration to 0.5 at. %.

Oshima *et al.* [102] have successfully addressed the impurity issues by designing a corrosion resistant HVPE reactor, and reported high-quality high-purity ScN epilayer growth on sapphire substrates. Mirrorlike homogeneous and stoichiometric ScN films with N/Sc ratio 1.01 ± 0.10 and thickness of up to 40 μm were deposited on *m*-plane and *r*-plane sapphire substrates with this method [see Fig. 2(c)]. The use of a corrosion resistant HVPE reactor suppressed the impurity concentrations including those of H, C, O, Si, and Cl. Due to the high purity of the film, and faster growth rates ranging at 100 s of $\mu m\,min^{-1}$, the *n*-type carrier concentration was reduced to a small value of $3.7 \times 10^{18}\,cm^{-3}$ and the carrier mobility also reached a high value of $284\,cm^2/V\,s$ for pure ScN films. Compared to high-quality GaN growth on sapphire substrates that require the deposition of low-temperature GaN or AlN as buffer layers, ScN growth does not require any seed layers. With purer reactants, it may also be possible to reduce the carrier concentrations to below $\sim 10^{18}\,cm^{-3}$ and increase the mobility of the films.

B. Molecular-beam epitaxy

In terms of the MBE growth, Smith *et al.* [80] deposited epitaxial ScN thin films on (001) MgO substrates by UHV MBE with a rf plasma source for nitrogen (N) and an effusion cell for scandium (Sc) at 800 °C. The flux ratio of Sc and N was found to play a crucial role in determining the structural, optical, and electronic properties of the deposited films. For N rich ($Sc/N < 1$) growth conditions, epitaxial and stoichiometric (001) oriented thin films were deposited, while for Sc rich ($Sc/N > 1$) growth conditions epitaxial yet nonstoichiometric films with nitrogen vacancies were obtained. STM imaging revealed that N_2 rich film surfaces possess square shaped plateaus and four-faced pyramids attributed to the spiral growth around dislocations. For Sc rich films, excess Sc on the top layer resulted in less distinct step edges compared to N_2 rich film, and surfaces exhibited metallic character [see Figs. 3(a) and 3(b)].

More recently Ohgaki *et al.* [104,105] reported the deposition of ScN on MgO (001) and α-Al_2O_3 ($1\bar{1}02$) substrates by radical source MBE using a rf plasma source for nitrogen. Hall measurements confirmed that MBE deposited ScN is a highly degenerate *n*-type semiconductor with carrier concentration ranging from 10^{19} to $10^{21}\,cm^{-3}$, and mobility ranging from 50 to $130\,cm^2/V\,s$. Their results also showed that mobility strongly depends on the growth temperature while the carrier concentration is independent of temperature variations.

Epitaxial ScN thin films with a cube-on-cube epitaxial relationship were deposited on Si (100) substrate by MBE methods by Moram *et al.* [106]. Results showed that the growth rate, surface roughness, and crystalline quality strongly depend on Sc flux rates. The growth surface was smooth initially, but with increasing film thickness (>50 nm) the surface roughness was increased due to the formation of square flat-topped islands attributed to higher growth rates and increase in grain sizes. Increase in mobility of the adatoms perhaps improved the crystalline quality, verified with a low full width

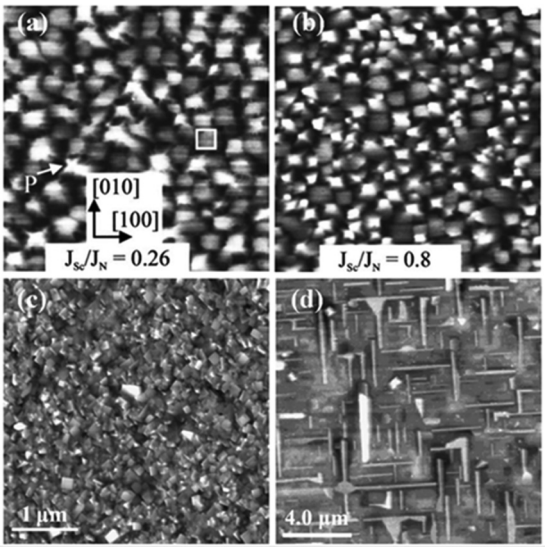

FIG. 3. (a) AFM images of ScN films deposited with Sc/N flux ratio 0.26 showing square shaped flat-topped mounds with a rms roughness of 19 Å (image size is $2 \times 2\,\mu$m). (b) AFM images of ScN thin film deposited with Sc/N flux ratio 0.80 showing pyramidal shaped and flat-topped mounds with a rms roughness of 21 Å (image size is $2 \times 2\,\mu$m). (c) AFM micrograph of ScN(100) grown on Si(100) at Sc flux ratio 4×10^{-7} mbar showing a rms roughness around 70 Å. (d) AFM images of films during initial nucleation of scandium silicide on Si substrate (100). Reproduced with permission from Refs. [80,103].

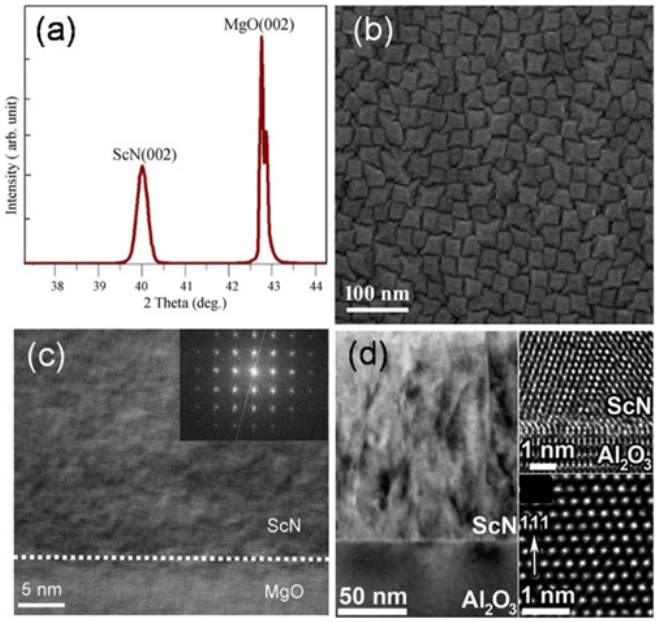

FIG. 4. (a) XRD spectrum of a sputter-deposited ScN thin film grown on (002) MgO substrates that demonstrate (002) oriented epitaxial crystal growth. (b) Plan view SEM image of the ScN surface exhibiting square flat-topped mounds with an average estimated feature size of 40 nm. (c) HRTEM micrograph of a ScN/MgO interface. Epitaxial cube-on-cube crystal growth was observed with signatures of misfit dislocations. (d) HRTEM micrograph of ScN thin film deposited on sapphire (Al_2O_3) substrates. Reproduced with permission from Refs. [82,83,86].

at half maximum (FWHM) of the rocking curve ($\sim 0.7^0$) at high Sc flux deposition conditions. Polycrystalline films oriented along [111] and [100] directions were obtained on Si (111) substrates [see Figs. 3(c) and 3(d)]. Electron cyclotron resonance MBE was also employed by Moustakas *et al.* [107] to deposit stoichiometric ScN thin films on sapphire substrates that exhibited absorption edges near 2.1 eV.

C. Magnetron sputtering and other deposition methods

Magnetron sputtering has been an attractive method for ScN thin-film deposition. In one of the earliest reports of sputter-deposited ScN, Gall *et al.* [77] showed polycrystalline thin-film growth on (001) MgO substrates with columnar grain structures having an average column separation of ~30 nm. Microscopy analysis revealed that though the films initially consisted of an approximately equal volume fraction of (002) and (111) oriented grains the film texture evolved through a kinetically limited competitive growth mode to complete (111) preferred orientations at larger critical thicknesses.

More recently, Burmistrova *et al.* [83] used dc-magnetron sputtering technique to deposit (002) oriented ScN thin films having a lattice constant of 4.50 Å on MgO(001) substrate at 850 °C substrate temperature [see Fig. 4(a)]. The highly textured films exhibited an x-ray rocking curve (ω-scan) FWHM of ~0.6°, which suggested good crystalline quality. Reciprocal space x-ray mapping (RSM) revealed that the films were epitaxial and fully strain relaxed with a mosaic spread of 0.086°, and SEM imaging of the surfaces showed the presence of densely packed squared grains with an average size of ~40 nm due to the formation of mound structures [see Fig. 4(b)]. As the film continues to grow those mounds connect along the edges, leading to the formation of cusps, which slows down the growth rate and increases surface roughness. Selective area electron diffraction confirmed [86] the epitaxial growth [see Fig. 4(c)] of ScN on MgO (001) substrates having an epitaxial relationship with ScN [001](001)‖MgO [001](001). Cube-on-cube crystal orientations were achieved in spite of a lattice mismatch of ~7% between ScN and MgO substrates.

The effects of deposition pressure on the microstructure of sputter-deposited ScN thin film were also studied [96]. For films deposited between 2 and 10 mTorr of deposition pressure, nominally single-crystalline ScN films having 002 oriented growth directions were achieved, which exhibited high thermoelectric power factors of 2×10^{-3} to 3.5×10^{-3} W/m K^2. The crystal quality and power factors, however, were significantly degraded for a higher deposition pressure at 20 mTorr due to the presence of (221) oriented secondary grains.

DC magnetron sputtering techniques were also employed to deposit ScN thin films on sapphire (0001) substrates [82]. The films grow with (111) orientations [see Fig. 4(d)] on the sapphire substrates, and exhibit an epitaxial relationship of ScN$\langle 1\bar{1}0\rangle \| Al_2O_3\langle 10\bar{1}0\rangle$ along the in-plane direction and ScN (111)‖Al_2O_3 (0001) along the out-of-plane direction. Cross-sectional microscopy imaging revealed [see Fig. 4(d)] columnar film domains and epitaxial ScN crystal growth on Al_2O_3 substrate, consistent with XRD analysis.

TABLE I. Electronic properties such as carrier concentration, mobility, and resistivity of ScN thin film deposited by various growth techniques and on different substrates.

Growth technique	Substrate	Carrier concentration (cm^{-3})	Mobility ($cm^2\,V^{-1}\,S^{-1}$)	Resistivity ($m\Omega\,cm$)	References
HVPE	α-Al_2O_3	0.9×10^{20}–47×10^{20}	0.3–176		Dismukes [72]
	Al_2O_3 *c*-, *m*-, *r*- and *a* planes, AlN *c*-plane (0001), GaN *c*-plane (0001), MgO, YSZ	10^{18}–10^{20}	284		Oshima *et al.* [102]
MBE	Sapphire(0001)	10^{17}–10^{19}	1–10		Moustakas *et al.* [107]
	MgO(001)	10^{21}		0.103–0.588	Smith *et al.* [80]
	MgO(001)	10^{19}–10^{21}	50–130		Ohgaki *et al.* [104]
Sputtering	MgO(001)			11–16	Gall and Petrov [76]
	MgO(001)	2.5×10^{20}	106	0.22	Burmistrova *et al.* [83]
	Al_2O_3 (0001)			0.29	Kerdsongpanya *et al.* [82]
	MgO(001)	10^{20}	18.6	2	Saha *et al.* [33]

IV. PHYSICAL PROPERTIES OF ScN

A. Electronic properties

Electronic properties of ScN have been investigated for several decades. During the early years of development in the 1960s–1970s, room-temperature electrical resistivities of 25, 130, 308, and 461 $\mu\Omega$ cm have been reported for ScN by Samsonov *et al.* [39], Sclar [88], Gschneider, Jr. [56], and Dismukes [72], respectively. Such low resistivity values were reminiscent of ScN's degenerate semiconducting or semimetallic characteristics due to the presence of defects. In 1972, Dismukes reported that HVPE deposited ScN films were *n*-type semiconductors with carrier concentration in the 10^{20}–$10^{21}\,cm^{-3}$ range, and mobility of $150\,cm^2/V\,s$. Similarly, early MBE-deposited ScN thin films [80] exhibited room-temperature electrical resistivity of 100–600 $\mu\Omega$ cm depending on the scandium to nitrogen flux ratio, and a high calculated carrier concentration of $\sim 10^{21}\,cm^{-3}$ from optical spectroscopic measurements. ScN thin films deposited with magnetron sputtering exhibited a room-temperature electrical resistivity of 12 mΩ cm, which is a factor of ~100–1000 higher than previous reports [72,88].

More recently, MBE-deposited ScN thin film by Ohgaki *et al.* [104] demonstrated high *n*-type carrier concentration in the 10^{19}–$10^{21}\,cm^{-3}$ range, and mobility between 50 and $130\,cm^2/V\,s$ (see Table I). Sputter-deposited ScN thin films by Burmistrova *et al.* [83] on MgO (001) substrate and by Kerdsongpanya *et al.* [82] on Al_2O_3(0001) substrate have exhibited carrier concentration and mobility of $2.5 \times 10^{20}\,cm^{-3}$ and $106\,cm^2/V\,s$, and $1 \times 10^{21}\,cm^{-3}$ and $30\,cm^2/V\,s$, respectively. Similarly as mentioned before, with a corrosion free HVPE reactor, Oshima *et al.* [102] showed that when the impurity level is significantly reduced stoichiometric ScN thin film exhibits electron concentrations ranging from 10^{18} to $10^{20}\,cm^{-3}$, and an extremely large mobility of $284\,cm^2/V\,s$.

Temperature-dependent electronic properties of ScN thin films have been also evaluated. Dismukes [72] found that with a decrease in temperature from 300 to 77 K carrier concentration of the HVPE deposited thin films changes by only 10%, which suggests that nearly all of the donor impurities remain ionized down to liquid nitrogen temperature. The mobility of films was found to decrease with an increase in temperature from 77 to 300 K, and exhibited $T^{-1.85}$ dependence for a carrier concentration of $1 \times 10^{20}\,cm^{-3}$, and $T^{-1.42}$ dependence for a carrier concentration of $2 \times 10^{21}\,cm^{-3}$. Such variations in mobility as a function of temperature were attributed to acoustic phonon scattering, which exhibits an otherwise ideal $T^{-1.5}$ dependence. Sputter-deposited ScN thin film by Gall and Petrov [76] exhibited decrease in the resistivity from $1.6 \times 10^{-2}\,\Omega\,cm$ at 80 K to $1.1 \times 10^{-2}\,\Omega\,cm$ at 400 K suggestive of its semiconducting nature.

Burmistrova *et al.* [83] and Kerdsongpanya *et al.* [82] have studied the electrical resistivity of ScN thin films at high temperatures in an effort to understand their thermoelectric properties, and found that the resistivity increases with an increase in temperature from 300 to 850 K. For ScN films deposited on MgO substrates, Burmistrova *et al.* [83] showed that the resistivity increased from $\sim 2 \times 10^{-4}\,\Omega\,cm$ at 300 K to $\sim 8 \times 10^{-4}\,\Omega\,cm$ at 850 K corresponding to an increase of about factor 4, while sputter-deposited ScN thin films on Al_2O_3 substrates exhibited much lower resistivity values, and a resistivity increase of about factor 2 with the same increase in temperatures. Saha *et al.* [86] have recently measured the temperature-dependent resistivity, mobility, and carrier concentrations of sputter-deposited ScN thin films at high temperatures (see Fig. 5), and found that with an increase in temperature from 300 to 850 K the mobility of the films decreases from ~70 to $\sim 20\,cm^2/V\,s$, thus exhibiting a $T^{-1.29}$ behavior. Therefore, the results suggest that acoustic impurity scattering is the most prevalent scattering mechanism for ScN thin films in the wide temperature ranges. The carrier concentration was also found to increase from 2.5×10^{20} to $4 \times 10^{20}\,cm^{-3}$ in the same temperature range, suggesting a thermal activation, albeit with a very small magnitude.

In terms of its electronic structure, ScN has been a subject of great interest for a long time. Early band-structure calculations by Nowotny and Neckel [108] and Weinberger *et al.* [109] had suggested that ScN is a semiconductor with band gaps of 0.6 and 0.1 eV, respectively, which were much smaller than the measured band gap from optical absorptions.

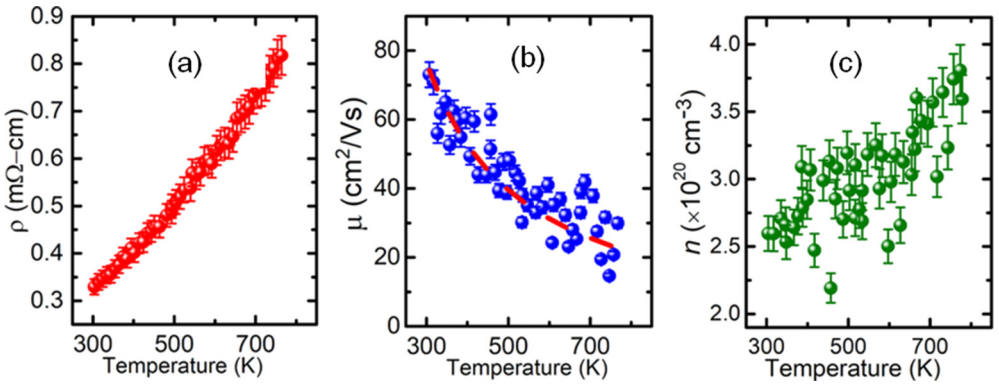

FIG. 5. Temperature-dependent (a) resistivity, (b) mobility, and (c) carrier concentration of sputter-deposited ScN thin film on MgO substrate. Reproduced with permission from Ref. [86].

Since it is well known that the traditional DFT calculations underestimate the band gap of semiconductors [110–113], several correction schemes such as screened exchange local-density approximation (LDA) [114], Hubbard U corrections [115], and GW methods [116] have been utilized to predict the correct band gap. Stampfl *et al.* [34] used screened exchange LDA and suggested an indirect Γ-X band gap of 1.58 eV, while Gall *et al.* [78] showed the indirect gap to be much smaller at 1.3 ± 0.1 eV (see Table II).The exact exchange DFT calculation of Gall *et al.* was in agreement with the XPS analysis, though a shift in the conduction band of 0.3 eV was necessary to match the experimental spectra. Using quasiparticle corrected local (spin) density functional calculation, Lambrecht [35] showed that the indirect band gap of ScN is a bit smaller at 0.9 eV. The quasiparticle corrections were estimated by assuming that the band-gap corrections are inversely proportional to the dielectric constant and using quasiparticle *d*-band shift in ErScAs. Though this approach results in an indirect band gap that is close to the experimental values, the dielectric constant disagreed significantly. Qteish *et al.* [32] used G_0W_0-quasiparticle calculations using exact-exchange Kohn-Sham density functional theory one-particle wave functions, and suggested that ScN has an indirect gap of 0.99 ± 0.15 eV. Band-structure calculations have showed that the top of the valence band in ScN is located at the Γ point, while the bottom of the conduction band is located at the X point of the Brillouin zone, leading to a Γ-X indirect band gap of 0.99 eV (see Fig. 6). Hubbard U corrections were also used to fit the band gap of ScN with experimental measurements. The calculated direct band-gap value at the Γ point, however, was significantly overestimated in such calculations compared to the experimental values. Screened exchange LDA calculations by Stampfl *et al.* [117] showed that for ScN the ideal-relaxed (001) surface has the lowest formation energy for most of the range of the allowed chemical potentials, and exhibits semiconducting properties with (1×1) structure. For the Sc rich growth condition, which is expected to result in N deficient structures, metallic conduction was predicted.

In the simplest picture of bonding, the scandium atom in ScN donates its two 4*s* electrons and single 3*d* electron to the nitrogen atom. Harrion and Straub [118] have suggested that in the rocksalt structure of ScN five *d* states of Sc hybridize with the three-valence *p* states of the neighboring nitrogen atom, forming three *p*-like bonding states, three *d*-like antibonding t_{2g} states, and two nonbonding e_g^2 states. The electronic densities of states have confirmed that the valence band of ScN is primarily dominated by nitrogen *p* states, which overlap with a fraction of the *d* states of Sc forming *p*-*d* hybridized states, while the lowest conduction band is mainly antibonding t_{2g}^3 3*d* states of scandium. The separation of these bonding and nonbonding states is the band gap, and is difficult to estimate with traditional Kohn-Sham DFT [119] based calculations.

TABLE II. First-principles density functional theory based analysis of the direct and indirect band gap, electron effective mass (m_t^* and m_l^*), and volume deformation potentials ($a_v^{\Gamma-X}$ and $a_v^{\Gamma-\Gamma}$) of ScN presented with various calculation methods.

Method	Indirect band gap (eV) (Γ-X)	Direct band gap (eV) (Γ-Γ)	Effective mass (m^*)		Volume deformation potential		References
			$m_t{}^*$	$m_l{}^*$	$a_v^{\Gamma-X}$	$a_v^{\Gamma-\Gamma}$	
ASA-LMTO	0.9						Lambrecht [35]
SX-LDA	1.58						Stampfl *et al.* [34]
EEX	1.3 ± 0.3						Gall *et al.* [78]
GGA + U(U = 3.5 eV)	0.89		0.281	2.061			Saha *et al.* [31]
$[G_0W_0]_{average}$	0.99	3.62					Qteish *et al.* [32]
OEPx(cLDA)-G_0W_0	0.84	3.51	0.189	1.483	2.02	1.54	
LDA-G_0W_0	1.14	3.71					
OEPx(cLDA)	1.70	4.53	0.253	1.450	2.06	1.07	
LDA, LDA-U^{SIC}	–0.15, 0.40	2.34, 3.25					

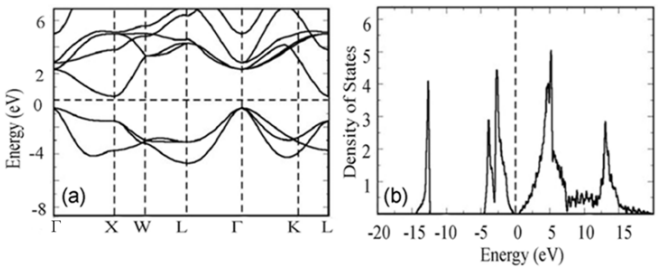

FIG. 6. (a) Electronic structure and (b) densities of electronic states of ScN calculated with DFT along with Hubbard U corrections. Reproduced with permission from Ref. [31].

To connect the electronic structure with its electrical transport characteristics, transverse (m_t^*) and longitudinal (m_l^*) conduction-band effective masses at the X point of the Brillouin zone and the volume deformation potentials were estimated [31,32]. GW calculations suggested [32] a transverse conduction-band effective mass of 0.189, while the generalized gradient approximation (GGA) along with the Hubbard U correction (with U = 3.5 eV) estimate indicate a bit larger m_t^* of 0.281 [31]. The m_l^* estimate varies from 1.625 to 2.031 in these calculations. The volume deformation potential, which holds critical information about the electronic structure of ScN deposited at different growth conditions, suggests that the direct Γ-Γ band-gap deformation potential is in the range 1.43–1.54, while the same for the indirect gap Γ-X was found to be typically in the range of 2.

B. Optical properties

Optical properties of ScN have been a topic of interest for a long time primarily to explore the prospect of utilizing them in optoelectronic devices. In one of the earliest reports of the spectroscopic analysis, Busch *et al.* [74] performed reflectance measurement on powders containing 80% of the theoretical nitrogen content of stoichiometric ScN, and observed a minimum in the absorption spectrum at an energy of 1.75 eV. Later research on HVPE deposited ScN thin films [72] showed [see Fig. 7(a)] that the free-carrier Drude absorption dominates in the long-wavelength region of the absorption spectrum, and varies as λ^2 (λ being the wavelength of incident light). The absorption spectrum [see Fig. 7(a)] showed an exponential dependence upon photon energy, and extended to both the lower and upper regions of the apparent band gap. High carrier concentration resulted in the perturbation of the band structure and exponential tailoring of the absorption spectrum, as a result of which it was not possible to determine the exact nature of its band-to-band transition. Nevertheless, the authors estimated a band-gap value of 2.1 eV from the dip in the absorption spectrum.

Subsequently MBE [80,120] and sputter-deposited [78] ScN thin films have exhibited a well-defined absorption edge at 2.15 and 2.37 eV, respectively, and with the advances of electronic structure calculations the nature the absorption edge was assigned to its direct band-gap Γ-Γ transition. The variation of the direct band gap as a function of carrier concentration was also measured by Deng *et al.* [121] with controlled fluorine impurity doping, and results showed [see Fig. 4(d)] that the direct band gap increases linearly from

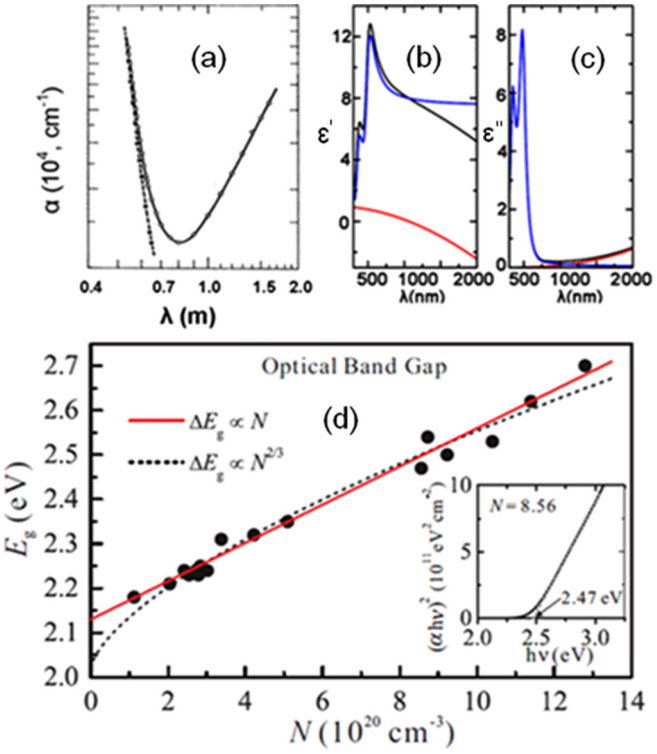

FIG. 7. (a) Dependence of optical absorption coefficient α upon wavelength λ at 300 K in HVPE deposited ScN thin film. (b) Real and (c) imaginary part of dielectric permittivity of ScN and (d) band gap vs carrier concentrations, obtained from Tauc's plot, as illustrated for $N = 8.56 \times 10^{20}$ cm^{-3} in the inset. Reproduced with permission from Refs. [33,72,121].

2.18 to 2.7 eV with an increase in carrier concentrations from 1.1×10^{20} to 12.8×10^{20} cm^{-3} due to Moss-Burstein shift.

While the estimation of direct band gap has been difficult due to ScN's large carrier concentration, accurate determination of its indirect gap was even more challenging. Apart from the fact that the absorption cross-section for indirect band-gap transition is quite small, large carrier concentration of the ScN films leads to Moss-Burstein shifts [122], which pushes the Fermi level to the bottom of the conduction band and makes the band diagram picture even more complicated. STM analysis performed on MBE deposited stoichiometric ScN films [120] showed an indirect band gap of ∼0.9 eV, while nitrogen deficient ScN films showed a similar gap of ∼0.95 eV, along with a second onset at 2.2 eV. These estimates of the indirect band gap were also verified by detailed absorption measurements [120], where indirect gap values between 0.9 and 1.2 eV were found.

Direct band-gap band-to-band transition at 2.2 eV was further demonstrated [33] by photoluminescence (PL) measurements from sputter-deposited ScN films grown on [001] MgO substrates. An emission peak at 2.2 eV with a FWHM of 0.25 eV was observed. The FWHM of the PL peak was much broader compared to well-known nitride semiconductors such as GaN and InN [123,124] possibly due to ScN's indirect band-gap nature. Though the exact mechanism of the observed PL remains to be explained, Saha *et al.* showed [33] that the intensity of the luminescence was proportional

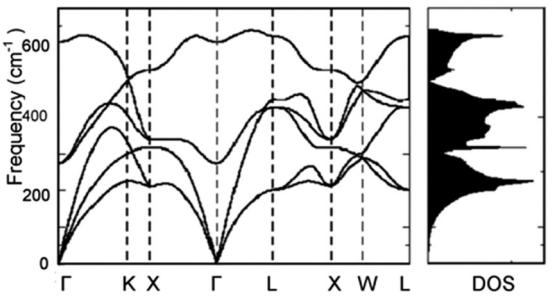

FIG. 8. Vibrational spectrum of ScN calculated with DFPT. The spectrum shows LO-TO splitting due to the polar nature of ScN. The densities of phonon states are also presented and exhibit no significant gap in the vibrational spectrum. Reproduced with permission from Ref. [31].

to the laser input power, suggestive of faster electron-hole recombination rates with respect to thermalization time of the electrons to the indirect X valley. Apart from ScN, several other indirect band-gap semiconductors such as Si and Ge exhibit similar PL characteristics due to interesting features in their band structure [125]. Therefore, it would be interesting to understand the underlying physical mechanism of PL in ScN. At the same time, since light emission at 2.2 eV is interesting and essential for addressing the yellow gap issue in solid-state lighting [126], ScN could become useful, though quantum yield measurements will be necessary.

Dielectric properties of ScN are also important for their optoelectronic applications. Spectroscopic ellipsometry based analysis showed [see Figs. 7(b) and 7(c)] that ScN behaves as a dielectric material in the visible to near IR wavelength range, with the real part of the dielectric permittivity at the interband transition position exhibiting a value of 12.8, which is consistent with previous first-principles based calculations [31]. Interestingly, Si also exhibits [127] a dielectric constant of 11.7 and indirect band gap of 1.1 eV, both of which are quite close to ScN. The long-wavelength regions of the permittivity spectrum were dominated by free electrons or Drude absorptions. The imaginary part of the dielectric permittivity showed a peak at ∼530 nm due to the band-to-band transitions, and increased in the long-wavelength range for free-electron absorptions.

C. Thermal properties

Compared to the electronic and optical properties, very little attention has been paid to determine the thermal properties of ScN. First-principles density functional perturbation theory [128,129] (DFPT) based modeling analysis of the vibrational spectrum showed [31] a LO and TO phonon splitting (∼335 cm^{-1}) at the Γ point of the Brillouin zone (see Fig. 8) resulting from long-range dipole-dipole interactions, representative of ScN's polar nature. Apart from such splitting of the optical phonon modes, both the LA and TA phonon modes softened along [001] and [111] directions due to the nesting of the Fermi surfaces by the wave vector (q). Debye temperature was also calculated from the vibrational spectrum to be 711 K, and calculations showed that at high temperatures the specific heat reaches an ideal Dulong-Petit value.

Boltzmann transport theory under a relaxation-time approximation [130,131] has been used to calculate the thermal

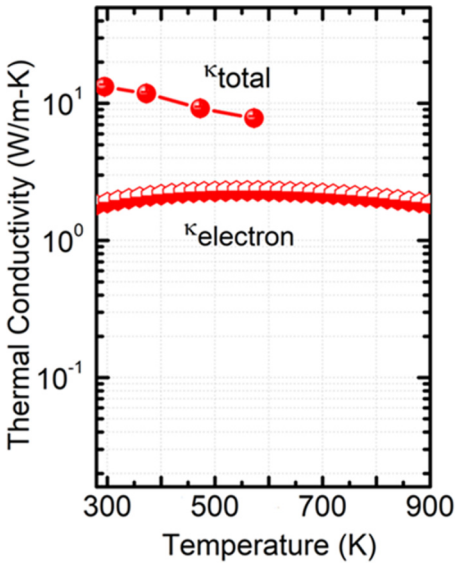

FIG. 9. Temperature-dependent thermal conductivity of ScN thin film deposited on MgO substrate, along with calculated electronic contribution to the total thermal conductivity. Reproduced with permission from Ref. [87].

conductivity of ScN from the full phonon dispersion spectrum (ω versus k) calculated with the DFPT [31], which showed that the acoustic phonons dominate thermal conductivity in ScN at lower temperatures. When the temperature is increased, the optical phonon mode starts contributing to the total thermal conductivity as expected. Since frequency and mode-dependent phonon relaxation time were not available, modeled thermal conductivity results could not be compared with experimental values. In a recent report, Kerdsongpanya *et al.* [132,133] have developed a theoretical model [134,135], which takes into account the effect of microstructure (grain size) of the ScN crystals and employed *ab-initio* descriptions that included temperature-dependent interatomic force constants, as well as anharmonic lattice vibrations. Prediction showed that with decreasing ScN thickness thermal conductivity should decrease due to smaller mean free paths of phonons allowed to transport, and demonstrated the effect experimentally with thin films deposited at different thicknesses. However, the predicted lattice thermal conductivity was a factor of 2 higher than the experimental results, which the authors attributed to the effects of point defects in experimental samples.

Time-domain thermoreflectance (TDTR) [136–138] has been utilized to measure the thermal conductivity of ScN thin films. Since ScN is a semiconductor with high electrical resistivity, the measured thermal conductivity should be primarily from lattice or phonon contributions, and the electronic component would be very small. Rawat *et al.* [61] have reported a room-temperature thermal conductivity of 10.6 W/m K in epitaxial ScN thin films of ∼300-nm thickness deposited on (001) MgO substrates. Temperature-dependent TDTR measurement technique showed (see Fig. 9) that the Umklapp scattering dominates thermal conductivity at higher temperatures with a scattering exponent of −0.85. Overall thermal conductivity decreased from 13.6 W/m K at 300 K to ∼7.5 W/m K at 550 K temperature.

D. Thermoelectric properties

Group III-nitride semiconductors (such as GaN, AlN, and InN) are traditionally regarded as inefficient thermoelectric materials since they exhibit low thermoelectric figures-of-merit (ZT) primarily due to their large thermal conductivities [16,139,140]. For example, GaN exhibits a room-temperature thermal conductivity in excess of 130 W/m K [141,142] while the room-temperature thermal conductivity of AlN is ∼320 W/m K [143]. Thermoelectric applications, however, require thermal conductivity to be as low as ∼1 W/m K [48,144–147]. In addition, several of the III nitrides generally do not exhibit necessary and important electronic properties for large thermoelectric power factors such as (a) asymmetry in the densities of electronic states at Fermi energy, (b) suitable carrier concentrations at $\sim 10^{19}$–10^{20} cm^{-3}, and (c) large effective mass of charge carriers.

Development of ScN has changed that scenario quite a lot. Early interest in ScN's thermoelectric properties dates back to the 1960s when Samsonov *et al.* [39] and Sclar [88] reported room-temperature Seebeck coefficients of −21 and −39 μV/K, respectively. The Seebeck coefficients were not that large perhaps due to the high degree of metallic characteristics that ScN exhibited in early years due to its substoichiometric nature, and the possible presence of defects. However, with the advances in thin-film deposition process, stoichiometric ScN thin films are deposited regularly albeit with unwanted impurity doping such as oxygen and fluorine, as well as nitrogen vacancies. These unwanted impurities act as electron donors, and result in a carrier concentration of $\sim 10^{19}$–10^{20} cm^{-3} in ScN, which is highly suitable to achieve large thermoelectric figures-of-merit.

Kerdsongpanya *et al.* [82] and Burmistrova *et al.* [83] have reported the thermoelectric properties of sputter-deposited ScN thin films grown on Al_2O_3 and MgO substrate, respectively. The room-temperature Seebeck coefficient was found to be −39 and −70 μV/K, respectively. With an increase in temperature from 300 to 800 K, Kerdsongpanya *et al.* [82] demonstrated that the Seebeck coefficient increases from ~ -39 to ~ -82 μV/K [see Fig. 10(a)], while similar increase in temperature from 300 to 850 K resulted in a Seebeck coefficient increase from ~ -70 to -160 μV/K in the thin films of ScN reported by Burmistrova *et al.* [83]. Due to such high Seebeck coefficient and moderately large electrical conductivity arising due to doping from impurities, thermoelectric power factors of the sputtered deposited ScN were extremely large, especially at high temperatures (∼600–850-K range). For ScN thin films deposited on Al_2O_3 substrates, Kerdsongpanya *et al.* [82] reported a high power factor value of 2.5×10^{-3} W/m K^2, while for films deposited on MgO substrates Burmistrova *et al.* [83] reported a power factor value of 3.3×10^{-3} W/m K^2 [see Fig. 10(b)]. Such power factors at 600–850-K temperature ranges are higher than the best known thermoelectric materials such as Bi_2Te_3 and its alloys at 400 K, as well as high-temperature thermoelectric materials such as La_3Te_4 at 600 K, and compare well with undoped crystalline SiGe in the same temperature range [148–150].

Despite such a large power factor, the overall thermoelectric figure-of-merit of ScN is quite low [83,87] at ∼0.2 at 800 K, due to its large thermal conductivity, which has been a limiting factor in its industrial applications for power generation or refrigeration applications. With the motivation to reduce thermal conductivity, Tureson *et al.* [151,152] and Kerdsongpanya *et al.* [153,154] have recently developed $Sc_{1-x}Nb_xN$ and $Sc_{1-x}Cr_xN$ solid solution alloys. In case of the $Sc_{1-x}Nb_xN$, the room-temperature thermal conductivity decreased from ∼10.5 W/m K for pure ScN down to a minimum value of 2.2 W/m K for $x = \sim 0.14$. However, the approximately five-factor decrease in thermal conductivity was also accompanied by a decrease of the thermoelectric power factors by a similar amount due to the decrease in the Seebeck coefficient and electrical conductivity, which led to an overall unchanged thermoelectric figure-of-merit. For $Sc_{1-x}Cr_xN$, the thermal conductivity decreased from ∼10.5 W/m K for pure ScN to as low as ∼2.3 W/m K for pure $Cr_{0.54}Sc_{0.46}N$ thin-film alloy. The Seebeck coefficients of alloy films were also found to increase with an increase in CrN concentrations inside $Sc_{1-x}Cr_xN$ alloys, which is suitable for thermoelectric applications. Electrical resistivity, however, was found to increase for the alloy films, which is detrimental for achieving high thermoelectric figure-of-merit. It must also be mentioned here that stoichiometric CrN thin films achieved by processing as-deposited films in a NH_3 gas environment exhibit a high thermoelectric power factor and figures-of-merit of 0.12–0.15 close to room-temperature [155,156]. Hole-type (*p*-type) carrier transport in nitrogen rich Al doped CrN thin films was

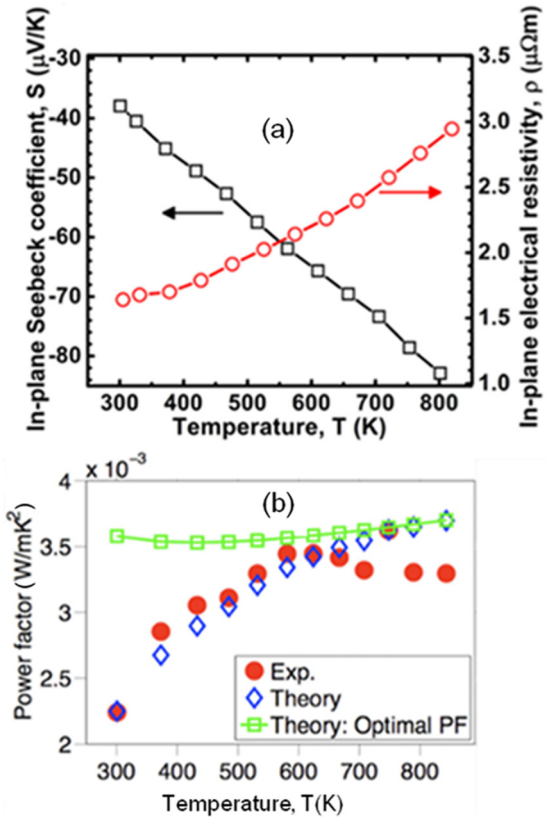

FIG. 10. (a) Seebeck coefficient and electrical resistivity of ScN as a function of temperature. (b) Power factor of ScN as a function of temperature. The maximum power factor of 3.5×10^{-3} (W/mK^2) was achieved at ∼600 K. Reproduced with permission from Refs. [82,83].

TABLE III. Mechanical properties including the hardness, Young modulus, Poisson ratio, and bulk modulus of ScN presented with experimental and theoretical/modeling results.

Method	Substrate	Hardness (GPa)	Young's modulus (GPa)	Poisson ratio	Bulk modulus B (GPa)	References
Experimental						
Sputtering	MgO(001)	12.9–25.7	287–408		182 ± 40	Gall *et al.* [77]
	TiN(001)/ MgO(001)			0.20 ± 0.04	187	Gall *et al.* [93]
MBE	Si(111)		270 ± 25	0.188 ± 0.1005		Moram *et al.* [106]
Theoretical/ modeling						
LDA and GGA		24.9	368.8	0.19	197.1	Liu *et al.* [172]
FPLMTO					210.364	Tebboune *et al.* [173]
			356	0.25	220	Meenaatci *et al.* [171]

also achieved in recent years, marking a significant progress in CrN based materials for thermoelectric applications [157]. Therefore, similar to the challenges encountered in most other thermoelectric materials systems [158–161], the reduction in thermal conductivity must be attained without reducing the power factor to achieve a higher thermoelectric figure-of-merit. In this regard, incorporation of nanoparticles [162–164], phase separation [165,166], a small amount of heavy element inclusion [167], and other approaches could be explored.

E. Mechanical properties

Like most other TMNs, the mechanical properties of ScN have been studied for over three to four decades to utilize its high hardness and large elastic modulus for tribology applications [168–170]. The valence electron density that determines the hardness of materials is the highest for ScN among group 3 nitrides, and as a result ScN thin films exhibit high mechanical hardness [171]. Gall *et al.* reported that (001) ScN thin films deposited on MgO substrates with MBE exhibit a hardness of 21.2 GPa, and an elastic modulus of 356 GPa at room temperature [77]. A bulk modulus of 182 GPa was also estimated with previously measured Poisson's ratio values. Subsequently, Moram *et al.* [106] reported a Young's modulus of 270 ± 25 GPa and Poisson's ratio of 0.188 ± 0.002 on (111) oriented ScN thin films deposited on Si substrates with MBE (see Table III).

Sputtered-deposited ScN (001) films grown on MgO substrate demonstrate a room-temperature hardness of 21 GPa and Young's modulus of 356 GPa, which is consistent with MBE-deposited ScN [77]. Sputter-deposited cubic-$Al_{0.72}Sc_{0.28}N$ thin-film alloys also exhibited a higher hardness to ~32 GPa, and cubic-$Ti_{0.5}Al_{0.36}Sc_{0.14}N$ solid solution alloys exhibited [174] an extraordinarily high hardness of 46 GPa. Though the exact mechanism of such high hardness is not clear, authors speculate that incorporation of ScN inside the $Ti_{1-x}Al_xN$ matrix improves the crystalline quality, thus leading to higher hardness values.

F. ScN as an interlayer for GaN growth

For solid-state lighting applications, ScN interlayers have been utilized to reduce the threading dislocation densities in GaN [53,81], that arise due to a large lattice mismatch (16%) between the film and the sapphire substrate. Threading dislocations are known to reduce efficiencies of GaN based lasers and light emitting diodes, act as nonradiative recombination centers reducing light emission efficiencies, and serve as scattering centers for charge carriers, thereby reducing the mobility of the films [139,175,176]. Typically GaN films deposited on sapphire substrates exhibit a threading dislocation density in excess of 5×10^9 cm^{-2} [177–179].

The lattice constant (a) of ScN is 4.50 Å, and the a lattice parameter for GaN is 3.18 Å which results in −0.1% lattice mismatch for (111) oriented cubic ScN and (0001) oriented hexagonal GaN [145]. Therefore, ScN interlayers should ideally reduce the threading dislocation density of GaN epilayers deposited on sapphire substrates. Using this hypothesis, Moram and coworkers [53,81] have demonstrated reduction of threading dislocation density in (0001) GaN from $(5.0 \pm 0.5) \times 10^9$ to $(3.1 \pm 0.4) \times 10^7$ cm^{-2} for coalesced films and to below 5×10^7 cm^{-2} for partially coalesced films [see Fig. 11(a)]. Microscopic analysis showed that ScN acts as an effective interlayer, and reduces the threading dislocation densities both for nonpolar $(11\bar{2}0)$ and semipolar $(11\bar{2}2)$ GaN films by orders of magnitude. In addition to reducing the threading dislocation densities, basal plane stacking faults were also significantly reduced [81] by the ScN interlayers.

The effect of ScN interlayer thickness on the threading dislocation density reduction was also studied [54] in coalesced GaN films, and results showed [see Fig. 11(b)] that with an increase in interlayer thickness from 2 to 12 nm the threading dislocation density reduced from 10.5×10^7 to 4.5×10^7 cm^{-2}. The films do not coalesce easily for an interlayer thickness of more than 15 nm, thus setting an upper limit of ScN interlayer thickness.

V. DEFECTS IN ScN: FIRST-PRINCIPLES THEORY AND EXPERIMENTS

Native defects and foreign impurities play a crucial role in determining the physical properties of semiconductors [180] and ScN is no exception. Thin-film growth techniques (such as magnetron sputtering, MBE, etc.) usually possess a background pressure arising from water vapor, O_2, CO_2, and other impurity gases that usually dope an otherwise intrinsic semiconductor with point defects such as vacancies, interstitials, antisite defects, etc. [181,182]. Similarly crystal

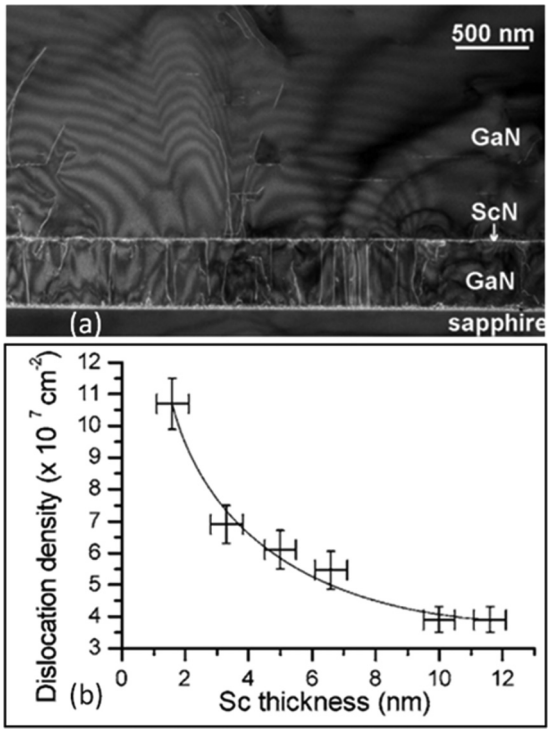

FIG. 11. (a) Threading dislocation density of GaN thin film was reduced by orders of magnitude with a ScN interlayer shown in this HRTEM micrograph. (b) Dislocation density is plotted as a function of ScN interlayer thickness, which showed that with an increase in interlayer thickness from 2 to 12 nm the dislocation density is reduced by a factor of ∼10. Reproduced with permission from Ref. [54].

structure, lattice constant, and surface and interface energy mismatch between the substrate and film result in extended defects such as dislocations, grain boundaries, stacking faults, etc. [183,184]. In the case of ScN, the effects of point defects (both native and foreign impurities) have been studied in a series of recent reports [185–187]. However, the nature and effects of the extended defects still require detailed analysis. In this section, we will address defects in ScN that are investigated by a combination of first-principles theory and experimental analysis.

A. Effect of nitrogen vacancy and other native defects

Nitrogen vacancies are a common point defect in many nitride semiconductors and affect their electronic as well as optoelectronic properties [138,188]. The presence of nitrogen vacancies was of great concern in the first few reports on ScN growth in the 1960s [40,74]. However, HVPE deposited ScN thin films by Dismukes [72] appeared to be relatively free from such defects based on three observations: (a) chemical analysis showed that HVPE deposited ScN films are stoichiometric and no gross deviation from the stoichiometry was observed for a range of deposited films; (b) no systematic increase in donor concentration was observed over the range of growth temperature 750–1150 °C; and (c) the donor concentration decreased with a decrease in ammonia and hydrogen halide concentration during the HVPE process. Following

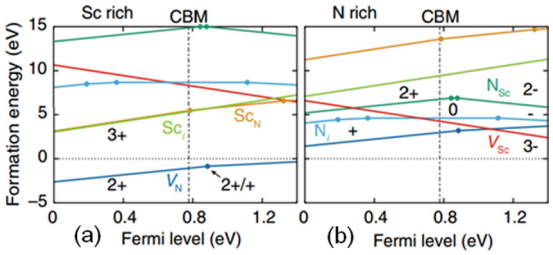

FIG. 12. DFT based calculation of native points defect formation energy in ScN. Reproduced with permission from Ref. [185].

this early work, XPS analysis by Porte [75] showed that ScN thin films prefer a stoichiometric condition, and growth of ScN in nitrogen deficient conditions results in stoichiometric ScN and metallic scandium mixtures, with no signature of any nitrogen deficient substoichiometric ScN. Therefore, their results indicated that nitrogen vacancy perhaps is not a favorable defect inside ScN.

More recently, Al-Brithen *et al.* [100] showed that for MBE grown ScN films stoichiometry is a strong function of the Sc/N flux ratio during the deposition process. For scandium rich conditions, the bulk Sc/N ratio approximately equals the flux ratio during the growth process; however, as the rocksalt structure of the crystal was maintained, it resulted in nitrogen vacancies. For nitrogen rich conditions, nitrogen vacancies were suppressed and the films were stoichiometric. Similarly, Oshima *et al.* [102] obtained stoichiometric ScN thin films with HVPE growth method, and Kerdsongpanya *et al.* [82] reported nearly stoichiometric films via magnetron sputtering.

Thermodynamics of nitrogen vacancy formation inside ScN have been calculated recently using first-principles DFT methods by Kumagai *et al.* [185] and presented in Fig. 12. Results showed that for Sc rich conditions nitrogen vacancy formation energy is negative in the entire range of Fermi energy, which could generate a large number of carriers (electrons). However, at N rich conditions, nitrogen vacancy energy was found to be positive, and it does not cause a Fermi-level pinning inside ScN's band gap. The thermodynamic analysis, therefore, is consistent with the experimental observations of MBE deposited ScN thin films by Al-Brithen *et al.* [100]. Calculation by Kumagai *et al.* [185] also showed that *p*-type doping in ScN is thermodynamically attainable as long as carrier compensation by unintentional impurities is well suppressed and a suitable hole dopant is chosen (see Fig. 13).

The nitrogen vacancy defect states are composed mainly of Sc e_g orbitals. Interestingly, the calculations revealed that only $V_N{}^{2+}$ emerges inside the band gap, which is not stable compared to the 1+ and 3+ charge states in traditional III-nitride semiconductors [189–191]. When the localized *d* orbitals constitute mainly the defect state, as with V_N in ScN, the on-site Coulomb repulsion is expected to be large. As a result, V_N preferentially accommodates only one electron, which is the reason why $V_N{}^{2+}$ is relatively stable in ScN. Electronic structure calculations [186] showed that nitrogen vacancies introduce an asymmetric peak close to the Fermi level in ScN, and the Fermi energy shifts from the band gap to the conduction-band edge.

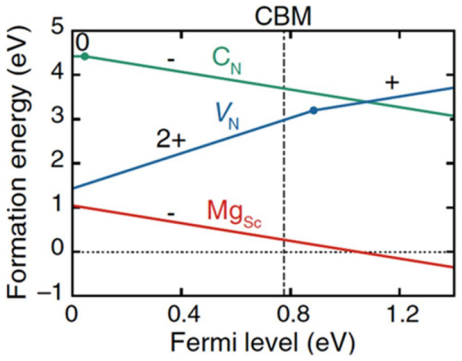

FIG. 13. Formation energy of *n*-type and *p*-type dopants inside ScN calculated by DFT based analysis. Mg incorporation energy in Sc atomic sites was found to be favorable, suggesting that *p*-type doping of ScN is possible. Reproduced with permission from Ref. [185].

Apart from nitrogen vacancy, the formation energies of other native point defects such as nitrogen or scandium interstitials, scandium vacancy, etc., were found to be quite large (see Fig. 12). Similarly antisite defect formation energies are also very high. Therefore, their effects could be neglected to a large extent.

B. Effect of oxygen impurity

Oxygen impurities in ScN originate primarily from source contaminations and background H_2O, O_2, and CO_2 gas concentrations during the thin-film deposition. Mass spectroscopic analysis of ScN thin films deposited with HVPE method [72] exhibited an O_2-impurity concentration of 4×10^{19} atoms/cm^{-3}. More recently, sputter-deposited ScN thin film [83] also exhibited 1.6 ± 1.0 at. % of oxygen, and for ScN films deposited on Al_2O_3 substrates [85] the oxygen-impurity content was lower at 0.3 at. %. Moram *et al.* [192] have showed that compared to other TMNs such as TiN, ZrN, etc., ScN is unusually susceptible to O_2 contaminations. Therefore, an in-depth understanding of the thermodynamics of oxygen-impurity formations inside ScN and its effects on the physical properties is necessary.

First-principles DFT [185] calculations have showed that the formation energies of oxygen impurity on the nitrogen atomic site (O_N) are energetically favorable across the whole range of Fermi energy (see Fig. 14). Oxygen impurities should also act as single donors. Therefore, experimentally observed oxygen impurities in HVPE or sputter-deposited ScN thin films are well explained by the thermodynamic analysis. With systematic variations of such impurity concentration in ScN, Burmistrova *et al.* [83] have showed that (a) the O_2-defect states do not reside inside the band gap of ScN, (b) there is no tendency of oxygen atoms to cluster and form precipitates, and (c) the presence of O_2 in ScN shifts the Fermi energy from ScN's band gap to its conduction-band edge. Such Moss-Burstein shift of the Fermi level was explained by the donor nature of oxygen impurities. Calculations have showed that for 1.56 at. % of O_2 inside ScN the Fermi level should be located at ~0.34 eV from the conduction-band edge.

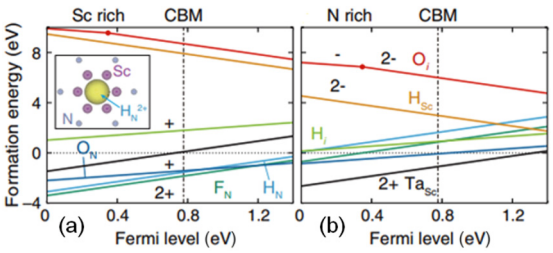

FIG. 14. DFT analysis of foreign impurity points defect formation energy in ScN. Results show that for oxygen, fluorine, and hydrogen impurities at nitrogen atomic sites the formation energies are negative, suggesting their possible presence in ScN films. Reproduced with permission from Ref. [185].

Moss-Burstein shift of the Fermi level to the conduction-band edge has enormous consequences on ScN's electronic properties. Measurements have showed that the electrical resistivity of ScN epilayers increases from 0.3 mΩ cm at 300 K to ~0.9 mΩ cm at 800 K [87], which represents its degenerate semiconducting or semimetallic transport behavior. Such transport characteristics can be well explained with the Moss-Burstein shift of the Fermi level. Similarly, the origins of high Seebeck coefficients and large thermoelectric power factors in sputter-deposited ScN thin film are also well explained by the Fermi-level position at the conduction-band edge. Boltzmann transport equation based modeling of Seebeck coefficients has showed that the experimental Seebeck coefficients could be well described for a Fermi-level position that is 0.06–0.09 eV above the conduction-band edge, which matches well with DFT calculations.

Moram *et al.* [192] also studied the effects of oxygen incorporation in ScN's optical and electronic properties by altering the deposition conditions and background pressure of ScN growth. Results showed that with an increase in the O_2 concentration direct band gap increased from 2.2 to ~3.1 eV, similar to the case of fluorine doped ScN [121], while the crystal structure degraded progressively with the incorporation of O_2. Oxygen contaminations also contributed to the non-Arrhenius behavior of ScN film's resistivity versus temperature behavior, and ultimately resulted in its degenerate *n*-type conductivity.

C. Effect of foreign impurities

Apart from the presence of native defects and oxygen impurities, several other foreign impurities such as fluorine [F], hydrogen [H], carbon [C], silicon [Si], tantalum [Ta], etc., have been observed in ScN films. Many of these foreign impurities arise from thin-film deposition processes related to reactant gas, metal precursors, sputtering targets, etc. For example, HVPE deposited ScN thin films in the early 1970s [72] contained 3×10^{19} cm^{-3} metal atom impurities arising mainly from [Si], [Fe], [Al], [Mg], and other rare-earth metals. Halogen impurities (such as chlorine [Cl] and others) were also found in HVPE deposited films arising from reactants. However, as mentioned before, in a recent report of HVPE deposited ScN [102], most of the metal impurity concentrations were effectively suppressed with a corrosion resistant reaction chamber.

For sputter-deposited ScN thin films, apart from O_2 contamination, the presence of [Ta] and [F] has been widely reported to arise potentially from sputtering targets. In the case of [F], processing of bulk ore used for target preparation, when the ore is etched by fluorine-containing acids to form an intermediate scandium fluoride step before obtaining scandium metal, introduces the impurities. Deng *et al.* [121] reported a [Ta] concentration of 0.04 ± 0.01 at. % in ScN, which was also observed in sputter-deposited ScN thin films [114]. [Ta] concentration remained relatively unchanged with respect to the changes in Ta-target lifetime. However, [F] concentration decreases from 3 ± 1 to <0.5 at. % over the sputter target lifetime.

The thermodynamics and defect formation energies of several of these foreign impurities have been calculated by Kumagai *et al.* [185]. Results showed that the formation energies of both the F_N and H_N impurities are negative for the whole range of Fermi-level position in Sc rich deposition conditions (see Fig. 14). F_N was found to be a double donor, consistent with recent observations that F_N doping introduces carrier electrons up to 1.3×10^{21} cm^{-3} in sputter-deposited ScN. Similarly, H_N impurities form a multicenter bonding with six Sc neighbors and act as a double donor, which is found in some other III-nitride semiconductors as well. At nitrogen rich conditions, H_N preferentially locates at the interstitial site near nitrogen with the N-H bond distance of 1.03 Å.

VI. COMPENSATION OF NATIVE DONOR DOPING IN ScN: *p*-TYPE $Sc_{1-x}Mg_xN$

Preferential doping of semiconductors with electron (*n*-type) and hole (*p*-type) carriers is one of the most fundamental requirements for its applications in solid-state devices such as *pn* junctions [193–195], light emitting diodes [196–198], semiconductor lasers [199,200], thermoelectric device modules [180,201], etc. Preferential *p*-type doping of wurtzite-nitride semiconductors such as GaN was challenging in the early years of its development. However, Amano *et al.* [202] demonstrated Mg doped *p*-type GaN growth by electron-beam irradiation, and later research by Nakamura *et al.* [203] demonstrated *p*-type GaN thin-film growth by annealing MOCVD deposited Mg doped GaN thin films inside N_2 and NH_3 environments. It is a well-established fact now that the development of *p*-type GaN was instrumental in GaN's eventual rise as perhaps the most famous nitride semiconductor, and paved the way for the demonstration of highly efficient light emitting diodes that transformed our society with solid-state lighting [204,205]. Therefore, for ScN to achieve wide scale industrial applications there is no doubt that preferential and easy to achieve *n*-type and *p*-type doping would be absolutely necessary.

All initial attempts to develop *p*-type ScN thin films in the 1970s were not successful. Dismukes [72] tried to deposit *p*-type ScN thin films during HVPE growth process by the addition of C and Si as dopants during the growth process. However, no *p*-type carrier conversion occurred, nor was the high electron concentration reduced. Further efforts to perform postgrowth annealing of ScN thin film at 1000 °C in the atmosphere of *p*-type dopants such as Zn or Mg or in vacuum were also not successful in achieving a *p*-type ScN film. Annealing of ScN in Zn-vapor for 1 h showed no appreciable changes on the electrical properties, while annealing in Mg-vapor reduced the carrier concentration from 2.3×10^{20} to 1.1×10^{20} cm^{-3} and significantly increased Hall mobility from 19 to 158 cm^2/V s. Annealing in vacuum, on the other hand, proved to be detrimental with an increase in electron concentration and reduction in carrier mobility. In no case could the authors achieve *p*-type doping in ScN thin film. Even though research in ScN stagnated for the next few decades, subsequent growth of ScN thin film with MBE and magnetron sputtering starting in the 1990s and early 2000s also did not address the *p*-type doping.

Saha *et al.* developed *p*-type ScN thin film by reactive magnetron cosputtering with the incorporation of Mg_xN_y [33] and Mn_xN_y [86] inside a ScN thin-film matrix. Physical properties of *p*-type $Sc_{1-x}Mg_xN$ and $Sc_{1-x}Mn_xN$ films were also studied with a motivation to develop electronic, optoelectronic, and thermoelectric devices. Results showed that with an initial increase in the Mg_xN_y concentration from 0 to ~2.5 at. % room-temperature resistivity of the $Sc_{1-x}Mg_xN$ films increased from ~0.3 to more than 7×10^3 mΩ cm, which amounts to a more than 10^4-factor increase (see Fig. 15). Such resistivity increase was also associated with decrease in the electron concentration from $\sim 6 \times 10^{20}$ cm^{-3} for undoped ScN thin film to $\sim 2 \times 10^{18}$ cm^{-3} for $x \sim 0.017$. Further increase in Mg_xN_y concentrations inside ScN film resulted in an electron-to-hole carrier type transition with resistivity decreasing to 2 mΩ cm with increased Mg_xN_y concentrations. Decrease in resistivity was associated with an increase in hole concentrations to a maximum 2.2×10^{20} cm^{-3} for *p*-type $Sc_{1-x}Mg_xN$ thin-film alloys. Hall mobility was found to decrease initially from ~63 cm^2/V s to less than ~5 cm^2/V s with an increase in Mg_xN_y content in the *n*-type carrier transport regime. However, mobilities recovered to a moderate 10–20 cm^2/V s range for samples with high hole concentrations.

Structural characterization of the $Sc_{1-x}Mg_xN$ thin films with high-resolution XRD and high-resolution transmission electron microscopy (HRTEM) also revealed [86] that the alloy films are substitutional solid solutions without any Mg_xN_y precipitations, phase separations, or secondary phase formations, and exhibited rocksalt crystal structure with lattice constants that are very close to that of undoped ScN. Optical characterization with UV-visible spectroscopy measurements showed direct band-gap optical absorption in pure ScN and in all *n*-type and *p*-type $Sc_{1-x}Mg_xN$ thin-film alloys. No signature of any sub-band-gap absorption was observed, which demonstrates that Mg_xN_y incorporation inside the ScN matrix does not add any defect states inside ScN's direct band gap or alter its basic band structure. The role of Mg doping was to act as an electron acceptor that reduces carrier concentration of pure ScN and eventually leads to *p*-type $Sc_{1-x}Mg_xN$ thin-film alloys. Irrespective of the carrier type, all $Sc_{1-x}Mg_xN$ thin-film alloys exhibited a direct gap of ~2.25 eV, which is the same as a direct band gap of pure ScN and supports the observation that the underlying electronic structure of ScN is unchanged after Mg_xN_y incorporation.

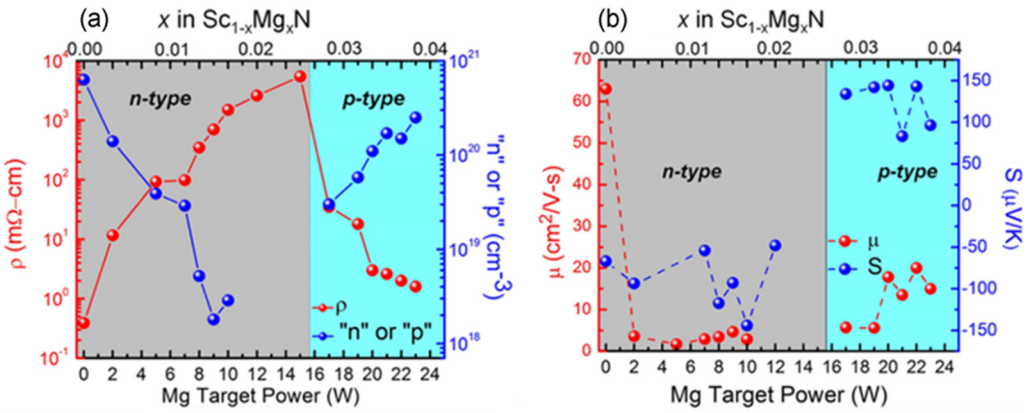

FIG. 15. (a) Variation of room-temperature resistivity (ρ) and carrier concentration (n or p) as a function of Mg target power and Mg_xN_y concentration inside the ScN matrix. (b) Variation of room-temperature mobility and Seebeck coefficient (S) as a function of Mg target power and Mg_xN_y concentration inside the ScN matrix. Reproduced with permission from Ref. [86].

Temperature-dependent resistivity measurements showed that with an increase in temperature from 300 to 850 K, and similar to the case of undoped ScN (see Fig. 5), p-type $Sc_{0.962}Mg_{0.038}N$ thin film (having the largest hole concentration) exhibits an increase in resistivity from ∼2.5 to ∼6 mΩ cm amounting to an approximately three-factor increase (see Fig. 16). Such increase in resistivity is representative of degenerate semiconducting or semimetallic nature. Subsequent modeling analysis revealed that heavy hole doping pushes the Fermi level inside the valence band of ScN, which gives rise to the increase in resistivity with the increase in temperature. It is similar to the case of undoped ScN, where unwanted oxygen impurities push the Fermi level from the middle of the band gap to inside the conduction band. Hall mobility of the films decreased from ∼20 to ∼8 $cm^2/V\,s$ corresponding to the same increase in temperature, and exhibited an exponent of −0.71, which is consistent with alloy scattering of holes at higher temperatures. The hole concentrations remained relatively unchanged with the increase in temperatures.

Temperature-dependent Seebeck coefficients and thermoelectric power factors of both n-type and p-type $Sc_{1-x}Mg_xN$ thin films have been investigated in detail [87], and results were explained with modeling analysis. All n-type and p-type $Sc_{1-x}Mg_xN$ thin films exhibited high Seebeck coefficient values. For p-type $Sc_{0.962}Mg_{0.038}N$, the Seebeck coefficient increased from ∼50 $\mu V/K$ at 300 K to ∼225 $\mu V/K$ at 850 K amounting to an approximately four-factor increase. Such large Seebeck coefficients resulted in high thermoelectric power factors of 7×10^{-4} to 8×10^{-4} $W/m\,K^2$ at 700–850 K in p-type $Sc_{0.962}Mg_{0.038}N$ thin film. Power factors of other p-type $Sc_{1-x}Mg_xN$ thin films were also large due to their high Seebeck coefficients.

Optimized power factors calculated by adjusting the carrier concentrations in n-type and p-type film showed (presented in Fig. 17) that the experimental power factors were close to the theoretically predicted optimum values, which meant that the carrier concentrations were already at the optimal level. Modeling analyses also revealed that for p-type $Sc_{0.962}Mg_{0.038}N$ thin film the Fermi level was ∼0.2 eV below the valence-band maxima, which is similar to the case for pure-ScN, where the Fermi level was found to be 0.06–0.12 eV above the conduction-band minima at 800 K. A plot of Fermi-level position with respect to the doping level in ScN at 800 K (presented in Fig. 17) also shows that the carrier concentrations for both n-type and p-type doping need to be reduced to below 3×10^{19} to 4×10^{19} cm^{-3} if the Fermi level is to be pushed inside the band gap.

The effects of p-type dopants on the electronic structure of ScN were also evaluated [186] using first-principles DFT based calculations. For nitrogen rich conditions Mg_{Sc} exhibited a shallow acceptor behavior. Furthermore, Mg_{Sc} was found to be lower in energy than V_N in the band gap, suggesting that Mg is a good acceptor dopant in ScN. Electronic structure calculations also revealed that for 3.125% Mg doping the Fermi level moves from the band gap to inside 0.4 eV below the valence-band maxima, which is consistent with experimental observations.

Apart from $Sc_{1-x}Mg_xN$, p-type $Sc_{1-x}Mn_xN$ thin-film alloys were also developed [33] with the incorporation of Mn_xN_y inside the ScN matrix. Mn doping was found to exhibit midgap defect states, and altered the basic band structure of ScN significantly. Moreover, the amount of Mn required to achieve p-type $Sc_{1-x}Mn_xN$ was also relatively larger in the 5.8 to 11% range. Nevertheless, both Mg and Mn doping in ScN proved to be effective for producing p-type ScN thin films, which will undoubtedly further the prospects of ScN based electronic and optoelectronic device technologies.

VII. ScN-WURTZITE (III-NITRIDE) ALLOYS

Several ScN-wurtzite (III-nitride) semiconductors [206] (such as wurtzite-$Al_{1-x}Sc_xN$, wurtzite-$Ga_{1-x}Sc_xN$, rocksalt-$Al_{1-x}Sc_xN$, etc.) have attracted interest in recent years for applications in piezoelectric materials [207] for surface and bulk acoustic resonators, micromachined ultrasound transducers [208], epitaxial metal/semiconductor superlattice growth [60,209], etc. In this section, we will discuss the physical properties of ScN (III-nitride) solid solution alloys.

A. Wurtzite $Al_{1-x}Sc_xN$: Piezoelectric materials and devices

As the demands for higher-temperature sensors are increasing drastically for applications in automobiles, aircrafts,

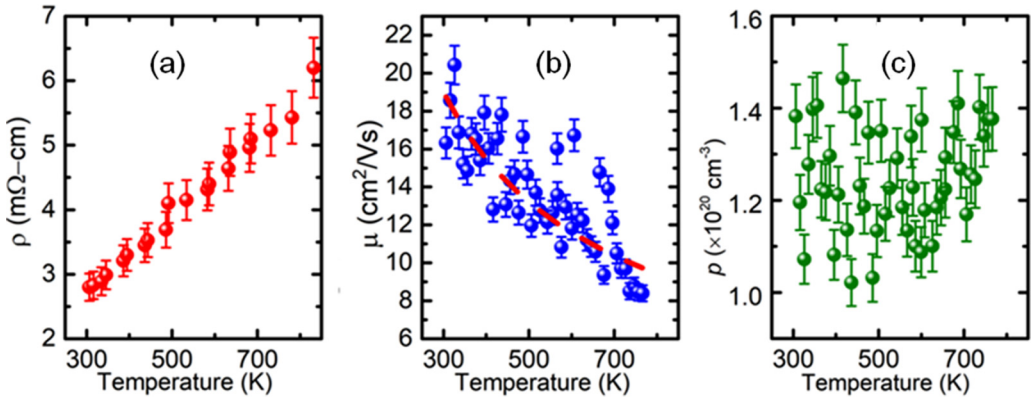

FIG. 16. Temperature-dependent (a) electrical resistivity, (b) mobility, and (c) carrier concentration of *p*-type $Sc_{0.962}Mg_{0.038}N$ alloy films. Reproduced with permission from Ref. [86].

turbine engines, monitoring of furnaces, turbine systems, etc., piezoelectric materials have become increasingly attractive and important [210–212]. It is a well-established phenomenon that materials with higher piezoelectric coefficients possess lower Curie temperatures [65,213]. For example, the Curie temperature and piezoelectric coefficient d_{33} of lead zirconium titanate (PZT), which is widely used in many electronic devices, are 250 °C and 410 pC N^{-1}, respectively [214]. Similarly, AlN exhibits a Curie temperature of 1150 °C, but with significantly lower piezoelectric coefficient d_{33} of 5.5 pC N^{-1} [215]. Therefore, designing materials that exhibit both higher Curie temperature and larger piezoelectric response will greatly improve many piezoelectric devices such as acoustic resonators, sensors, etc.

Among the III-nitride semiconductors, AlN exhibits the maximum piezoelectric coefficient and has already attracted significant interest for applications in micro-electromechanical (MEMS) devices. Akiyama *et al.* [65,213] demonstrated (see Fig. 18) that the piezoelectric coefficients of AlN can be increased by more than 400% with the incorporation of ScN inside the AlN matrix. The piezoelectric coefficient d_{33} of $Al_{1-x}Sc_xN$ alloy film was measured to be 27.6 pC N^{-1}, which is the highest among the reported tetrahedral bonded semiconductors. Moreover, the piezoelectric coefficients remained unchanged even after annealing the alloy at 550 °C for more than two days in vacuum. Piezoelectric properties of sputtered-deposited $Al_{1-x}Sc_xN$ thin films were also measured as a function of scandium nitride concentrations, which showed that the hexagonal intermediate phase of $Al_{1-x}Sc_xN$ alloys demonstrates the largest piezoelectric response.

The origin of such large enhancement in the piezoelectric response was investigated with first-principles DFT based calculations [63,207,216–219], which showed that the increase is an intrinsic alloying effect. Alloying was found to influence the energy surface topology, which leads to large elastic softening along the crystal parameter *c* and raises significantly the intrinsic sensitivity to axial strain that resulted in the enhanced piezoelectric coefficients. Modeling

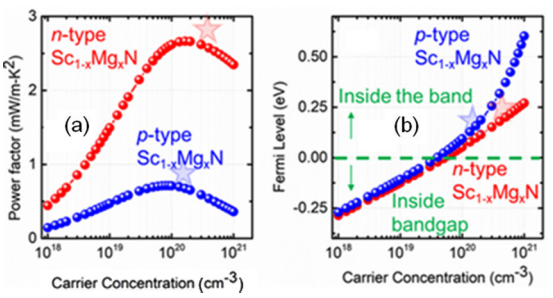

FIG. 17. Optimized (a) thermoelectric power factor and (b) Fermi energy plotted as a function of the *n*-type and *p*-type carrier concentrations inside ScN at 800 K. The Fermi energy positions are referenced with respect to the conduction- and valence-band edges. The figure shows that power factor values at high temperatures (800 K) are already optimized with respect to the carrier concentration in the *n*-type and *p*-type films. Reproduced with permission from Ref. [87].

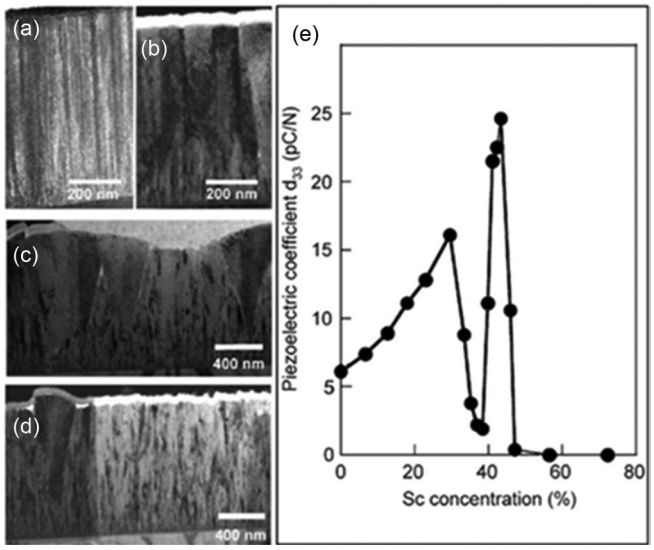

FIG. 18. Influence of Sc concentration on crystal growth of $Sc_xAl_{1-x}N$ alloys at Sc concentrations of (a) 41%, (b) 42%, (c) 43%, and (d) 45%. For Sc concentration below 41%, the structure is hexagonal, above 46% the structure is cubic, and between 42 and 45% both the cubic and hexagonal structure are present. (e) Variation of piezoelectric response d_{33} as a function of Sc concentration, showing maximum response at 43% Sc concentration. Reproduced with permission from Ref. [65].

also revealed that the flattening of the energy landscape was a consequence of the competition between the parent wurtzite and the so far experimentally undiscovered hexagonal phase of the $Al_{1-x}Sc_xN$ alloy that was responsible for this large enhancement in piezoelectricity.

$Al_{1-x}Sc_xN$ alloy based surface acoustic wave (SAW) devices with enhanced performance have also been demonstrated recently, highlighting their potential applications in MEMS based energy harvesting devices [26,67,220,221]. Compared to an AlN based SAW device, the $Al_{1-x}Sc_xN$ alloy devices exhibited much better transmission properties [222,223]. The electromechanical coupling coefficient K^2 was also found to be in the range between 2.0 and 2.2% for a wide normalized thickness range, which is a more than 300% increase when compared to that of an AlN based SAW device. Similarly, acoustic delay lines based on piezoelectric $Al_{1-x}Sc_xN$ thin-film hybrid transducers are also investigated [224] with modeling analyses. Results showed that such a novel hybrid resonator in which a bulk acoustic wave transforms into a SAW due to the special pillars patterned on the piezoelectric $Al_{1-x}Sc_xN$ thin film should be promising due to the high electromechanical coupling of greater than 4% [208,225].

B. Wurtzite $Ga_{1-x}Sc_xN$

$Ga_{1-x}Sc_xN$ alloy films have been developed [226,227] by the solid-state alloying between GaN and ScN mainly by MBE method, and exhibited different crystal structures depending on the ScN concentration inside the $Ga_{1-x}Sc_xN$ matrix [228–230]. Dismukes and Moustakas [231] showed that GaN and ScN should be highly soluble in one another in the rocksalt crystal structured $Ga_{1-x}Sc_xN$ phase, and the wurtzite crystal phase was stable for up to an intermediate ScN concentration. Calculations [229,232] also suggested a precise phase transition point at $x = 0.26$ for $Ga_{1-x}Sc_xN$ beyond which the alloy undergoes a wurtzite-to-rocksalt structural phase transition.

Little and Kordesch [233] used reactive magnetron sputtering to deposit $Ga_{1-x}Sc_xN$ alloy thin films on quartz substrates. XRD analysis revealed that the films exhibit amorphous and polycrystalline structure for $0.2 < x < 0.7$, and the direct band gap was found to decrease linearly from 3.5 to 2 eV with an increase in the ScN concentrations. Radio-frequency plasma nitrogen source MBE deposited films under nitrogen rich conditions revealed three crystal phases—(a) wurtzite-like ($x < 0.17$), (b) transitional ($0.17 < x < 0.54$), and (c) rocksalt ($x > 0.54$)—in $Ga_{1-x}Sc_xN$ thin films and a linear decrease in band gap with increasing ScN concentrations consistent with the observations by Little *et al.* (see [234]). MBE deposited $Ga_{1-x}Sc_xN$ thin-film alloys by Knoll *et al.* [230,235] contained high densities of *a*-type threading dislocations bent at the interfaces, which relax the misfit strains (see Fig. 19). All deposited films (having $x = 0.08$) were also found to be unintentionally *n* doped and PL measurements showed that they emit at 362 nm. Dislocation densities were found to be comparable to the GaN template and a significantly higher density of I_1-type basal plane stacking faults and planar defects were observed in the film with $x = 0.06$ [235,236].

Valence-band offsets between $Ga_{1-x}Sc_xN/AlN$ and $Ga_{1-x}Sc_xN/GaN$ heterojunctions were also measured with XPS based analysis [237,238]. Results showed that the valence-band offset for $Ga_{1-x}Sc_xN/AlN$ heterojunctions increased from 0.42 to 0.95 eV with an increase in the Sc concentration from 0 to 1.5%. Such increases in the band offsets were due to the internal distortions in bonding that result from the introduction of ScN into the GaN matrix [238]. The type-I band alignments in $Ga_{1-x}Sc_xN/AlN$ are suitable for UV optoelectronic applications [239,240]. On the other hand, type-II alignment was determined between the $Ga_{1-x}Sc_xN/GaN$ interfaces, which could expand the range of its applications [234,241–243].

C. Rocksalt $Al_{1-x}Sc_xN$

Unlike its wurtzite counterpart, rocksalt-$Al_{1-x}Sc_xN$ has attracted little attention [244,245]. Early reports [244,246] have showed that magnetron sputtered $Al_{1-x}Sc_xN$ alloy films deposited on sapphire and MgO substrates stabilize in rocksalt structure for maximum AlN mole fractions up to 60%. Further increase in AlN mole fractions leads to phase separation of $Al_{1-x}Sc_xN$ into rocksalt and wurtzite structures, before eventually converting the alloys into complete wurtzite structured grains [245,247,248]. Postgrowth annealing of $Al_{0.43}Sc_{0.57}N$ thin film at 1000–1100 °C also resulted in phase separations into nonisostructural cubic-ScN and wurtzite-structured AlN phase via nucleation and growth at grain boundaries due to volume mismatches. With an increase in AlN mole fraction from 0 to 50%, the lattice constants of the rocksalt-$Al_{1-x}Sc_xN$ alloy were found to decrease from 4.52 to 4.30 Å (see Fig. 20), which matches well with theoretical calculations. Such a decrease in lattice parameters is not surprising given that the stable rocksalt ScN exhibit a lattice constant of 4.52 Å, while rocksalt-AlN, though it is not stable at ambient conditions

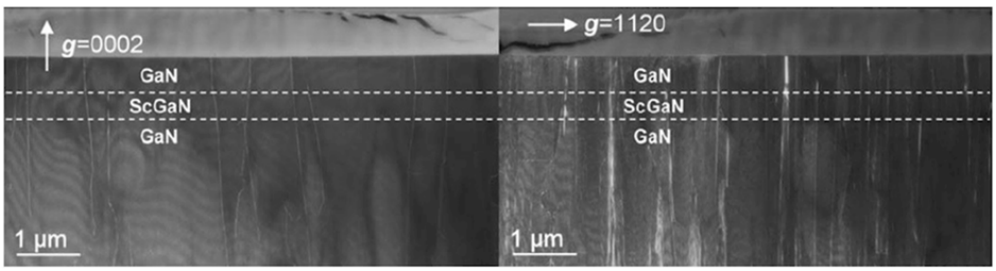

FIG. 19. Cross-sectional weak-beam dark field TEM images of $Sc_xGa_{1-x}N$ ($x = 0.08$) on the GaN template revealing c, (a+c) threading dislocations (0002) and a, (a+c) threading dislocations. Reproduced with permission from Ref. [226].

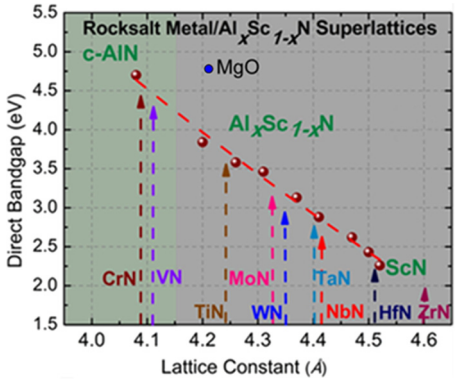

FIG. 20. Direct band gap of the rocksalt-$Al_xSc_{1-x}N$ alloys presented as a function of their lattice constants. Lattice parameters of the rocksalt metallic nitrides are also plotted in the same figure, which show that the rocksalt-$Al_xSc_{1-x}N$ can be lattice matched with most other metallic TMN for superlattice growth. Reproduced with permission from Ref. [60].

and can only be stabilized at high pressures, exhibits a lattice parameter of 4.08 Å [249–251].

The maximum AlN mole fraction required to stabilize $Al_{1-x}Sc_xN$ alloys in rocksalt phase was further increased from 60% to ∼84% with epitaxial stabilization technique by depositing a thin 20-nm TiN seed layer on (001) MgO substrates [60]. Reduced lattice mismatch at TiN/rocksalt-$Al_{1-x}Sc_xN$ interfaces and decreased bond polarity mismatches resulted in metastable rocksalt $Al_{1-x}Sc_xN$ alloy films with $0.62 < x < 0.82$. HRTEM imaging showed that rocksalt-$Al_{0.72}Sc_{0.28}N$ alloys grow with a cube-on-cube epitaxial relationship on TiN/MgO substrates without any signature of misfit dislocations. Critical thickness for stabilizing the rocksalt phase was found to exceed more than 120 nm for an $Al_{0.72}Sc_{0.28}N$ thin film deposited on 20-nm TiN/MgO substrate. At an AlN mole fraction of more than ∼84%, $Al_{1-x}Sc_xN$ thin films, however, undergo metastable-rocksalt to stable-wurtzite structural phase transition.

Microstructural evolution and epitaxial relationships during such metastable-rocksalt to stable-wurtzite structural phase transformation were also determined with HRTEM analysis [252]. An $Al_{1-x}Sc_xN$ alloy film was deposited on TiN/MgO substrates at a composition chosen to be at the phase boundary between the rocksalt and wurtzite phases, and a thin-film snapshot of the transformation was captured with HRTEM. Microstructural information revealed that the transformation was triggered by defects at the *rs*-$\{0\bar{1}1\}$ growth front that offer a nearly invariant plane with respect to the parallel *w*-$\{2\bar{1}\bar{1}0\}$ planes. Pyramidal rocksalt-$Al_{1-x}Sc_xN$ regions surrounded by the wurtzite-$Al_{1-x}Sc_xN$ matrix with twining relationships were also found. As most other III-nitride semiconductors exhibit a wurtzite-to-rocksalt structural phase transition upon applications of hydrostatic pressure inside diamond anvil cells, where a detailed microscopy analysis is not always feasible, the epitaxial and microstructural information obtained with $Al_{1-x}Sc_xN$ thin-film alloys is expected to carry over to such systems.

In terms of the electronic properties, with an increase in AlN content, resistivity of the $Al_{1-x}Sc_xN$ alloy films increased by more than two orders of magnitude within the rocksalt phase. A sharp decrease in the Hall mobility and appreciable changes in the carrier concentrations were also observed. However, as the alloys undergo the rocksalt-to-wurtzite structural phase transitions, the resistivity of the wurtzite films increased by six to ten orders of magnitude with an associated order-of-magnitude decrease in carrier concentrations. Similarly, optical properties such as direct band gap and dielectric permittivity of $Al_{1-x}Sc_xN$ alloy films were also evaluated [60]. The direct band gap was found to increase with increase in AlN mole fractions from 2.2 eV to ∼4 eV within the rocksalt crystal structure composition range, and exhibited a moderate band-gap bowing with a bowing parameter of 1.4 ± 0.19 eV, which is close to other III-nitride alloys such as (Al, Ga)N, (In, Ga)N, etc. Interpolation of the results also showed that rocksalt-AlN would exhibit a direct band gap of 4.70 ± 0.20 eV, which is close to the theoretical prediction of 4.99 eV. Spectroscopic ellipsometer measurements revealed that the dielectric permittivity of the $Al_{1-x}Sc_xN$ alloys decreases with an increase in the AlN mole fractions as expected.

VIII. METAL/SEMICONDUCTOR HETEROEPITAXY: (Zr,Hf)N/ScN MULTILAYERS AND TiN/(Al,Sc)N SUPERLATTICES

Defect-free and lattice-matched single-crystalline superlattice growth requires that the component materials (metallic and semiconducting layers) should exhibit several criteria such as (a) similarity in the crystal structure, (b) closely matched lattice constants, (c) low surface and interface energy density, etc. [253]. TMNs are composed of several metallic nitrides [27] (such as TiN, ZrN, HfN, VN, etc.) that exhibit rocksalt crystal structure with lattice constants varying from 4.05 to 4.60 Å (see Fig. 20). Therefore, the development of rocksalt-$Al_{1-x}Sc_xN$ with lattice constants ranging from 4.15 to 4.52 Å paves a way to lattice-match most of the TMN metals with rocksalt-$Al_{1-x}Sc_xN$ (see Fig. 20). For example, ScN ($a =$ 4.52 Å is lattice-matched to metallic HfN ($a = 4.52$ Å and has a very small mismatch with ZrN ($a = 4.59$ Å).

Epitaxial lattice-matched ZrN/ScN and HfN/ScN metal/semiconductor multilayers were deposited on (001) MgO substrates by reactive magnetron sputtering [61,84,254,255]. XRD analysis revealed that the multilayer films grow with (002) orientations, and exhibit *c*-axis lattice constants of 4.52 and 4.55 Å, respectively, which is an average of the individual layer's lattice parameters [61]. XRD also showed the presence of interference fringes suggestive of layer-by-layer epitaxial crystal growth with atomically sharp interfaces. Close inspection of the multilayer structures with HRTEM, however, revealed that ∼6% lattice mismatch between the nitrides and the MgO ($a = 4.21$ Å substrate results in threading dislocations that originate at the HfN/MgO interface and propagate through the films to the multilayer surfaces [84,256] (shown in Fig. 21). Due to the presence of such high densities of threading dislocations (10^{11} cm^{-2}) reproducible electrical measurements along the cross-plane directions were difficult to achieve.

Development of rocksalt-$Al_{1-x}Sc_xN$ alloy films has successfully addressed the lattice-mismatch issue and the

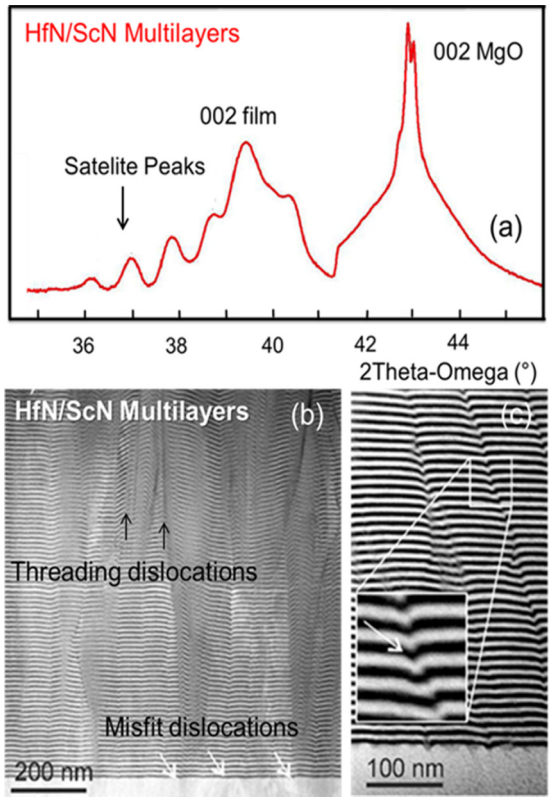

FIG. 21. (a) XRD spectrum of the HfN/ScN multilayer showing 002-oriented film growth. (b) HRTEM micrograph of the HfN/ScN multilayer showing threading dislocations that originate at the multilayer/MgO interface and propagate through the multilayers to the surface. (c) The inset from (b) shows that along the defect lines individual layers curve towards the MgO substrate. Reproduced with permission from Ref. [84].

associated effects of threading dislocations. Rocksalt-$Al_{1-x}Sc_xN$ with $x = 0.72$ exhibits a lattice constant $a = 4.25$ Å, which is very close to the lattice parameter of one of the most famous TMNs, TiN ($a = 4.24$ Å). At the same time, MgO substrate exhibits rocksalt structure and a lattice constant $a = 4.21$ Å, which is very close to the lattice parameters of the nitrides.

Epitaxial lattice-matched $TiN/Al_{0.72}Sc_{0.28}N$ metal/semiconductor superlattice heterostructures were deposited on (001) MgO substrates by UHV magnetron sputtering [59,60,257]. XRD analysis showed (see Fig. 22) that the films grow with (002) orientations with a very small (0.05°) FWHM of the rocking curve suggestive of a small degree of mosaicity. RSM exhibited that the asymmetric (024) peaks of the superlattice and MgO are all aligned vertically, which means that along the in-plane directions lattice constants of the substrate, TiN, and $Al_{0.72}Sc_{0.28}N$ are all fixed at 4.21 Å, while along the cross-plane directions only a slight relaxation was observed with TiN exhibiting a c-axis lattice constant of 4.23 Å and $Al_{0.72}Sc_{0.28}N$ alloys exhibiting a c-axis lattice constant of 4.25 Å. HRTEM imaging showed cube-on-cube epitaxial crystal growth with sharp and abrupt interfaces. Detailed characterization about thermal, optical, mechanical, and electronic properties of the superlattices was also performed [174,209,258], which highlighted the potential and suitability of such novel metamaterials in solid-state energy transport and conversion research fields such as in plasmonics [259–261], thermoelectricity [262–265], etc. However, a detailed discussion of the physical properties of the superlattices is beyond the scope of this research update and can be found in Ref. [266].

IX. CONCLUSION AND FUTURE PERSPECTIVE

In conclusion, scandium nitride (ScN) is an emerging rocksalt group 3-nitride semiconductor and shows promise for the next generation thermoelectric, electronic, and optoelectronic device technologies. Rocksalt (cubic) crystal structure, indirect band gap, and ability to preferentially dope ScN with n-type and p-type carriers will enable several electronic and optoelectronic devices with improved efficiencies. At the same time, successful demonstration of ScN based epitaxial metal/semiconductor heterostructure and superlattices is expected to innovate new physics concepts and device technologies. Though several challenges related to materials and devices remain to be addressed, here we will discuss a small number of opportunities in ScN research that would benefit development of ScN based practical device applications, including applications where ScN is expected to outperform other semiconducting materials.

A. Metallic nanoparticle inclusion in ScN for thermoelectric and terahertz applications

Epitaxial metallic nanoparticles embedded inside a semiconducting host demonstrate a range of interesting properties. For example, the presence of (semi) metallic nanoparticles can donate carriers, pin the Fermi level, shorten electron-hole recombination rates, enhance electron tunneling, and increase scattering of phonons in semiconductor host layers, which leads to efficient thermoelectric, plasmonic, and terahertz optoelectronic devices. Metallic nanoparticle inclusion inside ScN could improve its thermoelectric properties, as well as enable ScN based terahertz sources, detectors, and modulators. Heavy metal inclusion (such as W, Mo, or Hf) inside ScN would presumably reduce its thermal conductivity. Suitable metallic nanoparticles may also act as a Schottky barrier inside ScN that filters out low-energy electrons to increase the Seebeck coefficient, and hence improve its thermoelectric figure-of-merit. Similarly, metallic nanoparticle inclusion inside ScN (similar to the rare-earth semimetallic ErAs incorporation inside GaAs based III-arsenide semiconductors) could also result in photoconductive switches, detectors, etc., for terahertz optoelectronics with tunable spectral ranges [267,268].

B. ScN electronic devices

As ScN exhibited degenerate semiconducting or (semi) metallic characteristics with high carrier concentrations ($\sim 10^{20}$–10^{21} cm^{-3} at room temperature) for several decades, not much progress has been made in developing ScN based electronic devices such as diodes, transistors, etc. However, with the recent progress in hole doping that reduces carrier concentration, and development of p-type ScN thin film, it should be possible to develop basic electronic devices such

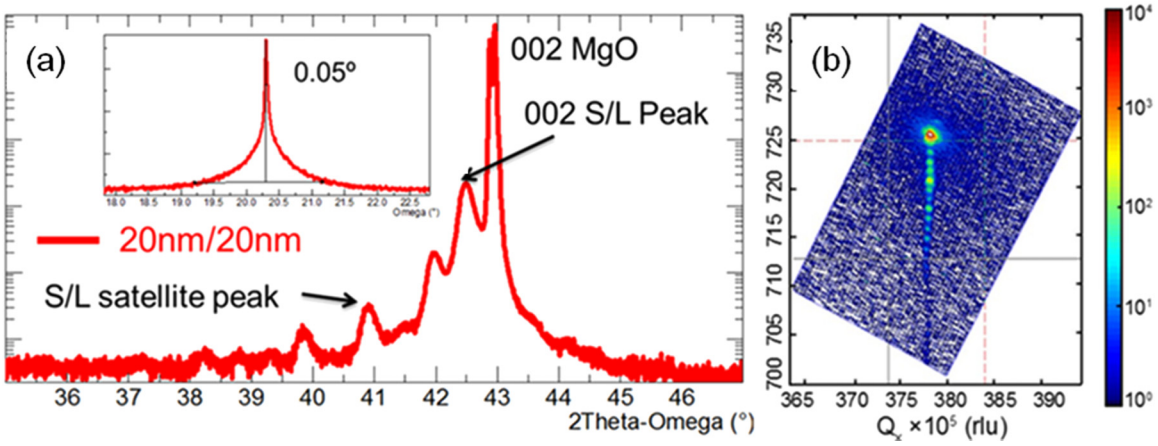

FIG. 22. XRD spectra of a 20-nm/20-nm $TiN/Al_{0.72}Sc_{0.28}N$ superlattice that exhibits 002-oriented growth. Superlattice satellite peaks are clearly observed indicating sharp interfaces. (b) Reciprocal space XRD map of the superlattice. Reproduced with permission from Ref. [257].

as *pn* junctions, Schottky barriers, and transistor devices with ScN as the semiconducting material. Since ScN exhibits an indirect band gap of ∼0.9 eV and dielectric permittivity of 12.3, which is similar to Si, it may be possible that ScN based electronic devices find some applications in industries.

C. Refractory electronics and plasmonics with ScN

Refractory materials [269] in materials science refer to those materials that exhibit (a) high melting temperatures (>2000 °C), (b) stability at high operating temperatures, retaining their physical and chemical properties, and (c) stable and preferential good contacts with other high-temperature materials. Such materials are useful in many industrial applications such as in combustion systems, well logging, industrial processes, supersonic aircrafts, and dense electronic packaging industries. A good refractory semiconducting material must exhibit several criteria, such as (a) large band gap, (b) ease of doping preferentially with *p*-type and *n*-type carriers, (c) large breakdown voltage, (d) ease of fabrication, as well as (e) preferential and stable Ohmic and Schottky contacts with other metals at high temperatures [270]. Due to such stringent requirements only a few semiconductors like diamond, SiC, and GaN are traditionally used as refractory semiconductors.

ScN exhibits a high melting temperature in excess of ∼2600 °C, and a direct band gap of 2.2 eV, and can be preferentially doped with both *n*-type and *p*-type carriers. Moreover, metal/ScN epitaxial contacts have also been developed (discussed earlier) that are stable at high operating conditions. Therefore, ScN and its heterostructures could be explored for high-temperature electronic applications. However, the band gap of ScN is not as large as that of the other well-known high-temperature materials and this might limit its applications to medium-temperature ranges. At the same time oxidation of ScN at high temperatures could be challenging. Therefore, much research effort will be needed to explore ScN's refractory applications, and effective coating materials and processing methods needs to be developed.

Integration of ScN with other transition-metal nitrides like TiN, ZrN, etc., may also lead to refractory plasmonic heterostructure devices for harvesting solar energy in solar photovoltaic and solar thermophotovoltaic devices [271–273]. For example, TiN is a promising alternative plasmonic material for Au in the visible spectral range, and $TiN/Al_{0.72}Sc_{0.28}N$ metal/semiconductor superlattices have demonstrated hyperbolic metamaterial properties. Their high-temperature properties could be investigated, which may result in promising refractory plasmonic devices with ScN as a component material.

ACKNOWLEDGMENT

The authors acknowledge financial support from International Centre for Materials Science in Jawaharlal Nehru Centre for Advanced Scientific Research.

[1] R. R. Schaller, IEEE Spectr. **34**, 52 (1997).
[2] Mark S. Lundstrom, Science **299**, 210 (2003).
[3] T. S. Cheung and J. R. Long, IEEE J. Solid-State Circuits **41**, 1183 (2006).
[4] J. R. Long and M. A. Copeland, IEEE J. Solid-State Circuits **32**, 357 (1997).
[5] J. C. Suhling and R. C. Jaeger, IEEE Sens. J. **1**, 14 (2001).
[6] D. Hartman, M. Grace, and C. Ryan, J. Lightwave Technol. **3**, 729 (1985).
[7] H. Iwai and S. Ohmi, Microelectronics Reliability **42**, 465 (2002).
[8] M. H. R. Lankhorst, B. W. S. M. M. Ketelaars, and R. A. M. Wolters, Nat. Mater. **4**, 347 (2005).
[9] R. J. Gutmann, IEEE Trans. Microw. Theory Tech. **47**, 667 (1999).
[10] T. D. Moustakas, T. Xu, C. Thomidis, A. Y. Nikiforov, L. Zhou, and D. J. Smith, Phys. Status Solidi Appl. Mater. Sci. **205**, 2560 (2008).
[11] Y. Huang, X. Duan, YI. Cui, and C. M. Lieber, Nano Lett. **2**, 101 (2002).
[12] S. Nakamura, T. Mukai, and M. Senoh, Appl. Phys. Lett. **64**, 1687 (1994).

[13] N. Shibata, Phys. Status Solidi A **192**, 254 (2002).
[14] H. J. Joyce, Q. Gao, H. H. Tan, C. Jagadish, and Y. Kim, Prog. Quantum Electron. **35**, 23 (2011).
[15] R. F. Davis, Proc. IEEE **79**, 702 (1991).
[16] S. Strite and H. Morkoç, J. Vac. Sci. Technol. B **10**, 1237 (1992).
[17] A. J. Turberfield, S. R. Haynes, P. A. Wright, R. A. Ford, R. G. Clark, J. F. Ryan, J. J. Harris, and C. T. Foxon, Phys. Rev. Lett. **65**, 637 (1990).
[18] S. Nakamura, M. Senoh, S. Nagahama, N. Iwasa, T. Yamada, T. Matsushita, H. Kiyoku, and Y. Sugimoto, Jpn. J. Appl. Phys. **35**, L74 (1996).
[19] S. Nakamura, M. Senoh, S. I. Nagahama, N. Iwasa, T. Yamada, T. Matsushita, H. Kiyoku, Y. Sugimoto, T. Kozaki, H. Umemoto, M. Sano, and K. Chocho, Appl. Phys. Lett. **72**, 211 (1998).
[20] D. L. Huffaker, G. Park, Z. Zou, O. B. Shchekin, and D. G. Deppe, Appl. Phys. Lett. **73**, 2564 (1998).
[21] J. Han, M. H. Crawford, R. J. Shul, J. J. Figiel, M. Banas, L. Zhang, Y. K. Song, H. Zhou, and A. V. Nurmikko, Appl. Phys. Lett. **73**, 1688 (1998).
[22] H. Page, C. Becker, A. Robertson, G. Glastre, V. Ortiz, and C. Sirtori, Appl. Phys. Lett. **78**, 3529 (2001).
[23] F. Qian, Y. Li, S. Gradec, and C. M. Lieber, Nano Lett. **4**, 1975 (2004).
[24] H. Kosaka, A. A. Kiselev, F. A. Baron, K. W. Kim, and E. Yablonovitch, Electron. Lett. **37**, 464 (2001).
[25] D. D. Awschalom, D. Loss, and N. Samarth, *Semiconductor Spintronics and Quantum Computation* (Springer, Berlin, 2002).
[26] P. Eklund, S. Kerdsongpanya, and B. Alling, J. Mater. Chem. C **4**, 3905 (2016).
[27] L. Toth (ed.), *Transition Metal Carbides and Nitrides* (Academic, New York, 1971).
[28] N. Takeuchi, Phys. Rev. B **65**, 045204 (2002).
[29] H. Shimizu, M. Shirai, and N. Suzuki, J. Phys. Soc. Jpn. **66**, 3147 (1997).
[30] W. Feng, S. Cui, H. Hu, G. Zhang, Z. Lv, and Z. Gong, Physica B **405**, 2599 (2010).
[31] B. Saha, J. Acharya, T. D. Sands, and U. V. Waghmare, J. Appl. Phys. **107**, 033715 (2010).
[32] A. Qteish, P. Rinke, M. Scheffler, and J. Neugebauer, Phys. Rev. B **74**, 245208 (2006).
[33] B. Saha, G. Naik, V. P. Drachev, A. Boltasseva, E. E. Marinero, and T. D. Sands, J. Appl. Phys. **114**, 063519 (2013).
[34] C. Stampfl, W. Mannstadt, R. Asahi, and A. J. Freeman, Phys. Rev. B **63**, 155106 (2001).
[35] W. R. L. Lambrecht, Phys. Rev. B **62**,13538 (2000).
[36] X. Bai and M. E. Kordesch, Appl. Surf. Sci. **175-176**, 499 (2001).
[37] W. Meissner and H. Franz, Z. Phys. **65**, 30 (1930).
[38] D. Geiselman, J. Less Common Met. **4**, 362 (1962).
[39] G. V. Samsonov, M. D. Lyutaya, and V. S. Netspor, Zh. Prikl. Khim. **36**, 2108 (1963) [Russ. J. Appl. Chem. **36**, 2043 (1963)].
[40] M. D. Lyutaya and V. F. Bukhanevich, Zhur. Neorg. Khim. **7**, 2487 (1962) [Russ. J. Inorg. Chem. **7**, 1290 (1962)].
[41] R. F. Voitovich and N. P. Shakhanova, Porosh. Met. **3**, 75 (1967) [Sov. Pwdr. Met. Metal Cer. **6**, 225 (1967)].
[42] L. Kaufman, Trans. AIME **224**, 1006 (1962).
[43] B. Saha, T. D. Sands, and U. V Waghmare, J. Phys.: Condens. Matter **24**, 415303 (2012).
[44] L. Khajavizadeh, Growth and structural characterization of ScN/CrN periodic and quasi-periodic superlattices for thermoelectric application, Master thesis, Linköping University, The Institute of Technology, 2014.
[45] J. L. Schroeder, D. A. Ewoldt, R. Amatya, R. J. Ram, A. Shakouri, and T. D. Sands, J. Microelectromechanical Syst. **23**, 672 (2014).
[46] A. Shakouri, Annu. Rev. Mater. Res. **41**, 399 (2011).
[47] J. M. Zide, D. O. Klenov, S. Stemmer, A. C. Gossard, G. Zeng, J. E. Bowers, D. Vashaee, and A. Shakouri, Appl. Phys. Lett. **87**, 112102 (2005).
[48] X. Shi, H. Kong, C.-P. Li, C. Uher, J. Yang, J. R. Salvador, H. Wang, L. Chen, and W. Zhang, Appl. Phys. Lett. **92**, 182101 (2008).
[49] C. F. Johnston, M. J. Kappers, M. A. Moram, J. L. Hollander, and C. J. Humphreys, J. Cryst. Growth **311**, 3295 (2009).
[50] S. Jang, H. Kim, D. Soo Kim, S.-M. Hwang, J. Kim, and K. Hyeon Baik, Appl. Phys. Lett. **103**, 162103 (2013).
[51] M. J. Kappers, M. A. Moram, Y. Zhang, M. E. Vickers, Z. H. Barber, and C. J. Humphreys, Physica B **401-402**, 296 (2007).
[52] M. A. Moram, M. J. Kappers, and C. J. Humphreys, Phys. Status Solidi C **7**, 1778 (2010).
[53] C. F. Johnston, M. A. Moram, M. J. Kappers, and C. J. Humphreys, Appl. Phys. Lett. **94**, 161109 (2009).
[54] M. A. Moram, Y. Zhang, M. J. Kappers, Z. H. Barber, and C. J. Humphreys, Appl. Phys. Lett. **91**, 152101 (2007).
[55] M. A. Moram, M. J. Kappers, T. B. Joyce, P. R. Chalker, Z. H. Barber, and C. J. Humphreys, J. Cryst. Growth **308**, 302 (2007).
[56] K. A. Gschneider, Jr., *Rare Earth Alloys* (Van Nostrand, Princeton, NJ, 1961).
[57] S. Adachi, *Properties of Semiconductor Alloys: Group-IV, III-V and II-VI Semiconductors* (Wiley, New York, 2009).
[58] M. Y. Shalaginov, V. V. Vorobyov, J. Liu, M. Ferrera, A. V. Akimov, A. Lagutchev, A. N. Smolyaninov, V. V. Klimov, J. Irudayaraj, A. V. Kildishev *et al.*, Laser Photon. Rev. **9**, 120 (2015).
[59] B. Saha, Y. R. Koh, J. Comparan, S. Sadasivam, J. L. Schroeder, M. Garbrecht, A. Mohammed, J. Birch, T. Fisher, A. Shakouri, and T. D. Sands, Phys. Rev. B **93**, 045311 (2016).
[60] B. Saha, S. Saber, G. V. Naik, A. Boltasseva, Eric A. Stach, Eric P. Kvam, and T. D. Sands, Phys. Status Solidi B **252**, 251 (2015).
[61] V. Rawat, Y. K. Koh, D. G. Cahill, and T. D. Sands, J. Appl. Phys. **105**, 024909 (2009).
[62] S. Mertin, V. Pashchenko, F. Parsapour, C. Nyffeler, C. S. Sandu, B. Heinz, O. Rattunde, G. Christmann, M. A. Dubois, and P. Muralt, in *2017 IEEE International Ultrasonics Symposium (IUS), Washington, DC* (IEEE, 2017), pp. 1–4.
[63] F. Tasnádi, B. Alling, C. Höglund, G. Wingqvist, J. Birch, L. Hultman, and I. A. Abrikosov, Phys. Rev. Lett. **104**, 137601 (2010).
[64] A. Zukauskaite, G. Wingqvist, J. Palisaitis, J. Jensen, Per O. Å. Persson, R. Matloub, P. Muralt, Y. Kim, J. Birch *et al.*, J. Appl. Phys. **111**, 093527 (2012).
[65] M. Akiyama, T. Kamohara, K. Kano, A. Teshigahara, Y. Takeuchi, and N. Kawahara, Adv. Mater. **21**, 593 (2009).

[66] P. Daoust, P. Desjardins, R. A. Masut, V. Gosselin, and M. Côté, Phys. Rev. Materials **1**, 055402 (2017).

[67] R. Matloub, M. Hadad, A. Mazzalai, N. Chidambaram, G. Moulard, C. S. Sandu, T. Metzger, and P. Muralt, Appl. Phys. Lett. **102**, 152903 (2013).

[68] N. M. Brooks, Found. Chem. **4**, 127 (2002).

[69] S. G. Brush, Isis **87**, 595 (1996).

[70] J. Emsley, Nat. Chem. **6**, 1025, (2014).

[71] R. Adunka and M. V. Orna, in *Carl Auer von Welsbach: Chemist, Inventor, Entrepreneur* (Springer, New York, 2018), pp. 17–34.

[72] J. P. Dismukes, J. Cryst. Growth **13**, 365 (1972).

[73] J. P. Dismukes, W. M. Yim, J. J. Tietjen, and R. E. Novak, J. Cryst. Growth **9**, 295 (1971).

[74] G. Busch, E. Kaldis, E. Schaufelberger-Teker, and P. Wächter, in *Les Filements des Terres Rares* (CNRS, Paris, 1970), Vol. 1, pp. 359–374.

[75] L. Porte, J. Phys. C **18**, 6701 (1985).

[76] D. Gall and I. Petrov, J. Vac. Sci. Technol. A **16**, 2411 (1998).

[77] D. Gall, I. Petrov, N. Hellgren, L. Hultman, J. E. Sundgren, and J. E. Greene, J. Appl. Phys. **84**, 6034 (1998).

[78] D. Gall, M. Städele, K. Järrendahl, I. Petrov, P. Desjardins, R. T. Haasch, T.-Y. Lee, and J. E. Greene, Phys. Rev. B **63**, 125119 (2001).

[79] F. Perjeru, X. Bai, and M. E. Kordesch, Appl. Phys. Lett. **80**, 995 (2002).

[80] A. R. Smith, H. A. H. Al-Brithen, D. C. Ingram, and D. Gall, J. Appl. Phys. **90**, 1809 (2001).

[81] M. A. Moram, C. F. Johnston, M. J. Kappers, and C. J. Humphreys, J. Cryst. Growth **311**, 3239 (2009).

[82] S. Kerdsongpanya, N. Van Nong, N. Pryds, A. Žukauskaite, J. Jensen, J. Birch, J. Lu, L. Hultman, G. Wingqvist, and P. Eklund, Appl. Phys. Lett. **99**, 232113 (2011).

[83] P. V. Burmistrova, J. Maassen, T. Favaloro, B. Saha, S. Salamat, Y. R. Koh, M. S. Lundstrom, A. Shakouri, and T. D. Sands, J. Appl. Phys. **113**, 153704 (2013).

[84] M. Garbrecht, J. L. Schroeder, L. Hultman, J. Birch, B. Saha, and T. D. Sands, J. Mater. Sci. **51**, 8250 (2016).

[85] B. Saha, Y. R. Koh, J. P. Feser, S. Sadasivam, T. S. Fisher, A. Shakouri, and T. D. Sands, J. Appl. Phys. **121**, 015109 (2017).

[86] B. Saha, M. Garbrecht, J. A. Perez-Taborda, M. H. Fawey, Y. R. Koh, A. Shakouri, M. Martin-Gonzalez, L. Hultman, and T. D. Sands, Appl. Phys. Lett. **110**, 252104 (2017).

[87] B. Saha, J. A. Perez-Taborda, J. H. Bahk, Y. R. Koh, A. Shakouri, M. Martin-Gonzalez, and T. D. Sands, Phys. Rev. B **97**, 085301 (2018).

[88] N. Sclar, J. Appl. Phys. **35**, 1534 (1964).

[89] W. Lengauer, J. Solid State Chem. **76**, 412 (1988).

[90] T. Bohnen, G. R. Yazdi, R. Yakimova, G. W. G. van Dreumel, P. R. Hageman, E. Vlieg, R. E. Algra, M. A. Verheijen, and J. H. Edgar, J. Cryst. Growth **311**, 3147 (2009).

[91] T. Bohnen, G. van Dreumel, P. Hageman, R. E. Algra, W. Enckevort, E. Vlieg, M. Verheijen, and J. H. Edgar, Phys. Status Solidi A **206**, 2809 (2009).

[92] J. H. Edgar, T. Bohnen, and P. R. Hageman, J. Cryst. Growth **310**, 1075 (2008).

[93] D. Gall, I. Petrov, P. Desjardins, and J. E. Greene, J. Appl. Phys. **86**, 5524 (1999).

[94] J. M. Gregoire, S. D. Kirby, G. E. Scopelianos, F. H. Lee, and R. B. Van Dover, J. Appl. Phys. **104**, 074913 (2008).

[95] R. T. Haasch, T.-Y. Lee, D. Gall, J. E. Greene, and I. Petrov, Surf. Sci. Spectra **7**, 178 (2000).

[96] P. V Burmistrova, D. N. Zakharov, T. Favaloro, A. Mohammed, E. A. Stach, A. Shakouri, and T. D. Sands, J. Mater. Res. **30**, 626 (2015).

[97] Z. Gu, J. H. Edgar, J. Pomeroy, M. Kuball, and D. W. Coffey, J. Mater. Sci. Mater. Electron. **15**, 555 (2004).

[98] H. A. Al-Atabi, N. Khan, Edil Nour, Joseph Mondoux, Yi Zhang, and J. H. Edgar, Appl. Phys. Lett. **113**, 122106 (2018).

[99] M. A. Moram, T. B. Joyce, P. R. Chalker, Z. H. Barber, and C. J. Humphreys, Appl. Surf. Sci. **252**, 8385 (2006).

[100] H. A. H. AL-Brithen, E. M. Trifan, D. C. Ingram, A. R. Smith, and D. Gall, J. Cryst. Growth **242**, 345 (2002).

[101] J. L. Hall, M. A. Moram, A. Sanchez, S. V Novikov, A. J. Kent, C. T. Foxon, C. J. Humphreys, and R. P. Campion, J. Cryst. Growth **311**, 2054 (2009).

[102] Y. Oshima, E. G. Víllora, and K. Shimamura, J. Appl. Phys. **115**, 153508 (2014).

[103] M. A. Moram, S. V. Novikov, A. J. Kent, C. Nörenberg, C. T. Foxon, and C. J. Humphreys, J. Cryst. Growth **310**, 2746 (2008).

[104] T. Ohgaki, K. Watanabe, Y. Adachi, I. Sakaguchi, S. Hishita, N. Ohashi, T. Ohgaki, K. Watanabe, Y. Adachi, I. Sakaguchi, and S. Hishita, J. Appl. Phys. **114**, 093704 (2013).

[105] T. Ohgaki, I. Sakaguchi, and N. Ohashi, Materials **11**, 2449 (2018).

[106] M. A. Moram, Z. H. Barber, C. J. Humphreys, T. B. Joyce, and P. R. Chalker, J. Appl. Phys. **100**, 023514 (2006)

[107] *Proceedings of the First Symposium on III-V Nitride Materials and Processes*, edited by T. D. Moustakas, J. P. Dismukes, and S. J. Pearton (The Electrochemical Society Inc., Pennington, NJ, 1996), Vol. 96, p. 197.

[108] H. Nowotny and A. Neckel, J. Inst. Metals **97**, 161 (1969).

[109] P. Weinberger, K. Schwarz, and A. Neckel, J. Phys. Chem. Solids **32**, 2063 (1971).

[110] W. Kohn, A. D. Becke, and R. G. Parr, J. Phys. Chem. **100**, 12974 (1996).

[111] A. J. Cohen, P. Mori-Sánchez, and W. T. Yang, Science **321**, 792, (2008).

[112] R. G. Parr, Proc. Natl. Acad. Sci. USA **76**, 2522 (1979).

[113] L. J. Sham and M. Schlüter, Phys. Rev. Lett. **51**, 1888 (1983).

[114] R. Asahi, W. Mannstadt, and A. J. Freeman, Phys. Rev. B **59**, 7486 (1999).

[115] P. Larson, W. R. L. Lambrecht, A. Chantis, and M. van Schilfgaarde, Phys. Rev. B **75**, 045114 (2007).

[116] F. Aryasetiawan and O. Gunnarsson, Reports Prog. Phys. **61**, 237 (1998).

[117] C. Stampfl, R. Asahi, and A. J. Freeman, Phys. Rev. B **65**, 161204(R) (2002).

[118] W. A. Harrison and G. K. Straub, Phys. Rev. B **36**, 2695 (1987).

[119] J. P. Perdew and M. Levy, Phys. Rev. Lett. **51**, 1884 (1983).

[120] H. A. Al-Brithen, A. R. Smith, and D. Gall, Phys. Rev. B **70**, 045303 (2004).

[121] R. Deng, B. D. Ozsdolay, P. Y. Zheng, S. V. Khare, and D. Gall, Phys. Rev. B **91**, 045104 (2015).

[122] J. Wu, W. Walukiewicz, W. Shan, K. M. Yu, J. W. Ager III, E. E. Haller, Hai Lu, and William J. Schaff, Phys. Rev. B **66**, 201403(R) (2002).

[123] K. Xu and A. Yoshikawa, Appl. Phys. Lett. **83**, 251 (2003).

[124] H. Tang and J. B. Webb, Appl. Phys. Lett. **74**, 2373 (1999).
[125] R. R. Lieten, K. Bustillo, T. Smets, E. Simoen, J. W. Ager III, E. E. Haller, and J.-P. Locquet, Phys. Rev. B **86**, 035204 (2012).
[126] P. M. Petroff, O. G. Lorimor, and J. M. Ralston, J. Appl. Phys. **47**, 1583 (1976).
[127] W. C. Dunlap and R. L. Watters, Phys. Rev. **92**, 1396 (1953).
[128] S. Baroni, S. De Gironcoli, A. Dal Corso, and P. Giannozzi, Rev. Mod. Phys. **73**, 515 (2001).
[129] K. Refson, P. R. Tulip, and S. J. Clark, Phys. Rev. B **73**, 155114 (2006).
[130] C. Jeong, R. Kim, M. Luisier, S. Datta, and M. Lundstrom, J. Appl. Phys. **107**, 023707 (2010)
[131] D. G. Cahill and W. K. Ford, J. Appl. Phys. **93**, 793 (2003).
[132] S. Kerdsongpanya, O. Hellman, B. Sun, Y. K. Koh, J. Lu, N. Van Nong, S. I. Simak, B. Alling, and P. Eklund, Phys. Rev. B **96**, 195417 (2017).
[133] O. Hellman, Peter Steneteg, I. A. Abrikosov, and S. I. Simak, Phys. Rev. B **87**, 104111 (2013).
[134] O. Hellman and I. A. Abrikosov, Phys. Rev. B **88**, 144301 (2013).
[135] O. Hellman, I. A. Abrikosov, and S. I. Simak, Phys. Rev. B **84**, 180301(R) (2011).
[136] P. Jiang, B. Huang, and Y. K. Koh, Rev. Sci. Instrum. **87**, 075101 (2016).
[137] Y. K. Koh, S. L. Singer, W. Kim, J. M. O. Zide, H. Lu, D. G. Cahill, A. Majumdar, and A. C. Gossard, J. Appl. Phys. **105**, 054303 (2009).
[138] H. J. Queisser and E. E. Haller, Science **281**, 945 (1998).
[139] J. Zou, D. Kotchetkov, A. A. Balandin, D. I. Florescu, and F. H. Pollak, J. Appl. Phys. **92**, 2534 (2002).
[140] M. D. Kamatagi, N. S. Sankeshwar, and B. G. Mulimani, Diam. Relat. Mater. **16**, 98 (2007).
[141] C.-Y. Luo, H. Marchand, D. R. Clarke, and S. P. DenBaars, Appl. Phys. Lett. **75**, 4151 (1999).
[142] E. Sichel and J. Pankove, J. Phys. Chem. Solids **38**, 330 (1977).
[143] H. Nakano, K. Watari, H. Hayashi, and K. Urabe, J. Am. Ceram. Soc. **85**, 3093 (2002).
[144] X. F. Zheng, C. X. Liu, Y. Y. Yan, and Q. Wang, Renew. Sustain. Energy Rev. **32**, 486 (2014).
[145] S. B. Riffat and X. Ma, Appl. Therm. Eng. **23**, 913 (2003).
[146] K. Biswas, J. He, I. D. Blum, C.-I. Wu, T. P. Hogan, D. N. Seidman, V. P. Dravid, and M. G. Kanatzidis, Nature (London) **489**, 414 (2012).
[147] L.-D. Zhao, S.-H. Lo, Y. Zhang, H. Sun, G. Tan, C. Uher, C. Wolverton, V. P. Dravid, and M. G. Kanatzidis, Nature (London) **508**, 373 (2014).
[148] H. Takiguchi, A. Matoba, K. Sasaki, Y. Okamoto, H. Miyazaki, and J. Morimoto, Mater. Trans. **51**, 878 (2010).
[149] Y. Wang, Y. J. Hu, X. Chong, J. P. S. Palma, S. A. Firdosy, K. E. Star, J. P. Fleurial, V. A. Ravi, S. Shanga, and L. Chena, Comput. Mater. Sci. **142**, 417 (2018).
[150] I. Malika, S. Banerjeea, C. Gaynera, A. Chowdhuria, and K. K. Kar, Ceram. Int. **44**, 10685 (2018).
[151] N. Tureson, N. Van Nong, D. Fournier, N. Singh, S. Acharya, S. Schmidt, L. Belliard, A. Soni, A. le Febvrier, and P. Eklund, J. Appl. Phys. **122**, 025116 (2017).
[152] N. Tureson, M. Marteau, T. Cabioch, N. Van Nong, J. Jensen, J. Lu, G. Greczynski, D. Fournier, N. Singh, A. Soni, L. Belliard, P. Eklund, and A. le Febvrier, Phys. Rev B **98**, 205307 (2018).
[153] S. Kerdsongpanya, B. Sun, F. Eriksson, J. Jensen, J. Lu, Y. K. Koh, N. Van Nong, B. Balke, B. Alling, and P. Eklund, J. Appl. Phys. **120**, 215103 (2016).
[154] S. Kerdsongpanya, B. Alling, and P. Eklund, J. Appl. Phys. **114**, 073512 (2013).
[155] C. X. Quintela, J. P. Podkaminer, M. N. Luckyanova, T. R. Paudel, E. L. Thies, D. A. Hillsberry, D. A. Tenne, E. Y. Tsymbal, G. Chen, C. Eom, and F. Rivadulla, Adv. Mater. **27**, 3032 (2015).
[156] M. A. Gharavi, S. Kerdsongpanya, S. Schmidt, F. Eriksson, N. V. Nong, J. Lu, B. Balke, D. Fournier, L. Belliard, A. Le Febvrier, C. Pallier, and P. Eklund, J. Phys. D **51**, 355302 (2018).
[157] A. L. Febvrier, N. V. Nong, G. Abadias, and P. Eklund, Appl. Phys. Express **11**, 051003 (2018).
[158] H. J. Goldsmid and G. S. Nolas, in *Proceedings ICT2001. 20th International Conference on Thermoelectrics (Cat. No. 01TH8589), Beijing, China* (IEEE, 2001), pp. 1–6.
[159] G. J. Snyder and E. S. Toberer, Nat. Mater. **7**, 105 (2008).
[160] J.-F. Li, W.-S. Liu, L.-D. Zhao, and M. Zhou, NPG Asia Mater. **2**, 152 (2010).
[161] M. S. Dresselhaus, G. Chen, M. Y. Tang, R. Yang, H. Lee, D Wang, Z. Ren, J. P. Fleurial, and P. Gogna, Adv. Mater. **19**, 1043 (2007).
[162] M. A. Scarpulla, J. M. O. Zide, J. M. LeBeau, C. G. de Walle, A. C. Gossard, and K. T. Delaney, Appl. Phys. Lett. **92**, 173116 (2008).
[163] M. Zebarjadi, K. Esfarjani, A. Shakouri, Z. Bian, J.-H. Bahk, G. Zeng, J. Bowers, H. Lu, J. Zide, and A. Gossard, J. Electron. Mater. **38**, 954 (2009).
[164] W. Kim, J. Zide, A. Gossard, D. Klenov, S. Stemmer, A. Shakouri, and A. Majumdar, Phys. Rev. Lett. **96**, 045901 (2006).
[165] M. Samanta and K. Biswas, J. Am. Chem. Soc. **139**, 9382 (2017).
[166] L.-D. Zhao, S.-H. Lo, J. He, H. Li, K. Biswas, J. Androulakis, C.-I. Wu, T. P. Hogan, D.-Y. Chung, V. P. Dravid, and M. G. Kanatzidis, J. Am. Chem. Soc. **133**, 20476 (2011).
[167] C. X. Quintela, B. Rodriguez-Gonzalez, and F. Rivadulla, Appl. Phys. Lett. **104**, 022103 (2014).
[168] A. Grill, Surf. Coatings Technol. **94-95**, 507 (1997).
[169] C. Donnet, Surf. Coatings Technol. **100-101**, 180 (1998).
[170] K. V. Chauhan and S. K. Rawal, Procedia Technol. **14**, 430 (2014).
[171] A. T. A. Meenaatci, R. Rajeswarapalanichamy, and K. Iyakutti, Phase Transitions **86**, 570 (2013).
[172] Z. T. Y. Liu, X. Zhou, S. V Khare, and D. Gall, J. Phys.: Condens. Matter **26**, 025404 (2014).
[173] A. Tebboune, D. Rached, A. Nour Benzair, Nadir Sekkal, and A. H. Belbachir, Phys. Status Solidi B **243**, 2788 (2006).
[174] B. Saha, S. K. Lawrence, J. L. Schroeder, J. Birch, D. F. Bahr, and T. D. Sands, Appl. Phys. Lett. **105**, 151904 (2014).
[175] J. W. P. Hsu, M. J. Manfra, S. N. G. Chu, C. H. Chen, L. N. Pfeiffer, and R. J. Molnar, Appl. Phys. Lett. **78**, 3980 (2001).
[176] L. Sugiura, J. Appl. Phys. **81**, 1633 (1997).
[177] P. Visconti, K. M. Jones, M. A. Reshchikov, R. Cingolani, H. Morkoç, and R. J. Molnar, Appl. Phys. Lett. **77**, 3532 (2000).

[178] C. Youtsey, L. T. Romano, R. J. Molnar, and I. Adesida, Appl. Phys. Lett. **74**, 3537 (1999)

[179] X. Q. Shen, H. Matsuhata, and H. Okumura, Appl. Phys. Lett. **86**, 021912 (2005).

[180] M. Jang, M. S. Jun, T. M. Roh, J. D. Kim, and T. H. Zyung, US Patent No. 2002/0187020 A1 (27 May 2010).

[181] Sokrates T. Pantelides, Rev. Mod. Phys. **50**, 797 (1978).

[182] W. Walukiewicz, Appl. Phys. Lett. **54**, 2094 (1989).

[183] W. Schröter, J. Kronewitz, U. Gnauert, F. Riedel, and M. Seibt, Phys. Rev. B **52**, 13726 (1995).

[184] D. Holt and B. Yacobi, *Extended Defects in Semiconductors: Electronic Properties, Device Effects and Structures*, 1st ed. (Cambridge University, Cambridge, England, 2007).

[185] Y. Kumagai, N. Tsunoda, and F. Oba, Phys. Rev. Appl. **9**, 034019 (2018)

[186] S. Kerdsongpanya, B. Alling, and P. Eklund, Phys. Rev. B **86**, 195140 (2012).

[187] A. L. Febvrier, N. Tureson, N. Stilkerich, G. Greczynski, and P. Eklund, J. Phys. D **52**, 035302 (2018).

[188] E. Yamaguchi and M. R. Junnarkar, J. Cryst. Growth **189-190**, 570 (1998).

[189] Y. Kumagai, K. Harada, H. Akamatsu, K. Matsuzaki, and F. Oba, Phys. Rev. Appl. **8**, 14015 (2017).

[190] A. Janotti, J. L. Lyons, and C. G. Van de Walle, Phys. Status Solidi A **209**, 65 (2012).

[191] C. G. de Walle and J. Neugebauer, J. Appl. Phys. **95**, 3851 (2004).

[192] M. A. Moram, Z. H. Barber, and C. J. Humphreys, Thin Solid Films **516**, 8569 (2008).

[193] E. Monroy, E. Muñoz, F. J. Sánchez, F. Calle, E. Calleja, B. Beaumont, P. Gibart, J. A. Muñoz, and F. Cussó, Semicond. Sci. Technol. **13**, 1042 (1998).

[194] S. Nakamura, M. Senoh, and T. Mukai, Jpn. J. Appl. Phys. **30**, L1708 (1991).

[195] P. Muralt, Appl. Phys. Lett. **49**, 1441 (1986).

[196] S. Nakamura, T. Mukai, and M. Senoh, Jpn. J. Appl. Phys. **30**, L1998 (1991).

[197] K. Y. Ko, J. W. Kim, D. W. Kim, H. J. Park, S. M. Hwang, and S. W. Chae, US Patent No. 8,110,847 B2 (7 February 2012).

[198] L. P. Sadwick, US Patent No. 8,502,454 B2 (6 August 2013).

[199] D. Meschede, *Optics, Light, and Lasers, The Practical Approach to Modern Aspects of Photonics and Laser Physics* (Wiley-VCH, Weinheim, Germany, 2017).

[200] Z. Fang, C. Haiwen, G. Chen, and R. Qu, *Fundamentals of Semiconductor Lasers* (Springer, New York, 2017), pp. 9–39.

[201] S. Sharma, V. K. Dwivedi, and S. N. Pandit, Inter. J. Green Energy **11**, 899 (2014).

[202] H. Amano, M. Kito, K. Hiramatsu, and I. Akasaki, Jpn. J. Appl. Phys. **28**, L2112 (1989).

[203] S. Nakamura, T. Mukai, M. Senoh, and N. Iwasa, Jpn. J. Appl. Phys. **31**, L139 (1992).

[204] C. Humphreys, MRS Bull. **33**, 459 (2008).

[205] S. Nakamura, MRS Bull. **34**, 101 (2009).

[206] M. A. Moram and S. Zhang, J. Mater. Chem. A **2**, 6042 (2014).

[207] M. A. Caro, S. Zhang, T. Riekkinen, M. Ylilammi, M. A. Moram, O. Lopez-Acevedo, J. Molarius, and T. Laurila, J. Phys. Condens. Matter **27**, 245901 (2015).

[208] Q. Wang, Y. Lu, S. Fung, X. Jiang, S. Mishin, Y. Oshmyansky, and D. A. Horsley, Proc. Solid-State Sensor **1**, 9 (2016)

[209] B. Saha, G. V. Naik, S. Saber, C. Akatay, E. A. Stach, V. M. Shalaev, A. Boltasseva, and T. D. Sands, Phys. Rev. B **90**, 125420 (2014).

[210] D. Damjanovic, Curr. Opin. Solid State Mater. Sci. **3**, 469 (1998).

[211] S. Zhang, R. Xia, L. Lebrun, D. Anderson, and T. R. Shrout, Mater. Lett. **59**, 3471 (2005).

[212] Z. Shujun and Y. Fapeng, J. Am. Ceram. Soc. **94**, 3153 (2011).

[213] M. Akiyama, K. Kano, and A. Teshigahara, Appl. Phys. Lett. **95**, 162107 (2009.)

[214] Y. Saito, H. Takao, T. Tani, T. Nonoyama, K. Takatori, T. Homma, T. Nagaya, and M. Nakamura, Nature (London) **432**, 84 (2004).

[215] R. C. Turner, P. A. Fuierer, R. E. Newnham, and T. R. Shrout, Appl. Acoust. **41**, 299 (1994).

[216] Y. Bin Jia, Adv. Mater. Res. **690-693**, 1698 (2013).

[217] C. Tholander, F. Tasnádi, I. A. Abrikosov, L. Hultman, J. Birch, and B. Alling, Phys. Rev. B **92**, 174119 (2015).

[218] H. Berkok, A. Tebboune, A. Saim, and A. H. Belbachir, Physica B **411**, 1 (2013).

[219] S. Zhang, D. Holec, W. Y. Fu, C. J. Humphreys, and M. A. Moram, J. Appl. Phys. **114**, 133510 (2013).

[220] Tang Gongbin, Investigation on high performance surface acoustic devices using ScALN thin films, Ph.D. thesis, Chiba University, Japan, 2017, https://core.ac.uk/download/pdf/96950343.pdf.

[221] S. Fichtner, T. Reimer, S. Chemnitz, F. Lofink, and B. Wagner, APL Mater. **3**, 116102 (2015).

[222] W. Wang, P. M. Mayrhofer, X. He, M. Gillinger, Z. Ye, X. Wang, A. Bittner, U. Schmid, and J. K. Luo, Appl. Phys. Lett. **105**, 133502 (2014).

[223] V. Pashchenko, R. Matloub, F. Parsapourkolour, P. Muralt, S. Ballandras, and K. Haffner, in *2016 IEEE International Ultrasonics Symposium (IUS), Tours, France* (IEEE, 2016), pp. 1–4.

[224] Q. Wang, Y. Lu, S. Mishin, Y. Oshmyansky, and D. A. Horsley, J. Microelectromech. Sys. **26**, 1132 (2017).

[225] V. Pashchenko, S. Mertin, F. Parsapour, J. Li, P. Muralt, and S. Ballandras, in *2017 Joint Conference of the European Frequency and Time Forum and IEEE International Frequency Control Symposium (EFTF/IFCS), Besancon, France* (IEEE, 2017), pp. 565–566.

[226] M. A. Moram, Y. Zhang, T. B. Joyce, D. Holec, P. R. Chalker, P. H. Mayrhofer, M. J. Kappers, and C. J. Humphreys, J. Appl. Phys. **106**, 113533 (2009).

[227] C. Constantin, J. Pak, K. Wang, A. Chinchore, M. Shi, and A. R. Smith, MRS Proc. **1202**, 1202-I05-25 (2009).

[228] S. Zhang, W. Y. Fu, D. Holec, C. J. Humphreys, and M. A. Moram, J. Appl. Phys. **114**, 243516 (2013).

[229] C. Constantin, M. B. Haider, D. Ingram, A. R. Smith, Na. Sandler, K. Sun, and P. Ordejón, J. Appl. Phys. **98**, 123501 (2005).

[230] S. M. Knoll, S. Zhang, T. B. Joyce, M. J. Kappers, C. J. Humphreys, and M. A. Moram, Phys. Status Solidi A **209**, 33 (2012).

[231] J. P. Dismukes and T. D. Moustakas, in *Proceedings of the First Symposium on III-V Nitride Materials and Processes* (The Electrochemical Society, Pennington, NJ, 1996), Vol. 96, p. 110.

[232] H. C. L. Tsui, L. E. Goff, N. P. Barradas, E. Alves, S. Pereira, H. E. Beere, I. Farrer, C. A. Nicoll, D. A. Ritchie, and M. A. Moram, Phys. Status Solidi A **212**, 2837 (2015)
[233] M. E. Little and M. E. Kordesch, Appl. Phys. Lett. **78**, 2891 (2001)
[234] J. Schrier, D. O. Demchenko, Lin-Wang, and A. P. Alivisatos, Nano Lett. **7**, 2377 (2007).
[235] S. M. Knoll, S. K. Rhode, S. Zhang, T. B. Joyce, and M. A. Moram, Appl. Phys. Lett. **104**, 101906 (2014).
[236] S. M. Knoll, M. Rovezzi, S. Zhang, T. B. Joyce, and M. A. Moram, J. Phys.: Condens. Matter **26**, 225801 (2014).
[237] E. A. Kraut, R. W. Grant, J. R. Waldrop, and S. P. Kowalczyk, Phys. Rev. Lett. **44**, 1620 (1980).
[238] H. C. L. Tsui, L. E. Goff, R. G. Palgrave, H. E. Beere, I. Farrer, D. A. Ritchie, and M. A. Moram, J. Phys. D **49**, 265110 (2016).
[239] A. Franciosi and C. G. Van de Walle, Surf. Sci. Rep. **25**, 1 (1996).
[240] H. Kroemer, Phys. Scr. **1996**, 10 (1996).
[241] W. Snodgrass, B. R. Wu, W. Hafez, K. Y. Cheng, and M. Feng, IEEE Electron Device Lett. **27**, 84 (2006).
[242] O. M. Nayfeh, C. N. Chleirigh, J. Hennessy, L. Gomez, J. L. Hoyt, and D. A. Antoniadis, IEEE Electron Device Lett. **29**, 1074 (2008).
[243] J. Kang, S. Tongay, J. Zhou, J. Li, and J. Wu, Appl. Phys. Lett. **102**, 012111 (2013).
[244] C. Höglund, J. Birch, B. Alling, J. Bareño, Z. Czigány, Per O. Å. Persson, G. Wingqvist, A. Zukauskaite, and L. Hultman, J. Appl. Phys. **107**, 123515 (2010).
[245] C. Höglund, B. Alling, J. Birch, M. Beckers, Per O. Å. Persson, C. Baehtz, Z. Czigány, J. Jensen, and L. Hultman, Phys. Rev. B **81**, 224101 (2010).
[246] C. Höglund, J. Bareño, J. Birch, B. Alling, Z. Czigány, and L. Hultman, J. Appl. Phys. **105**, 113517 (2009).
[247] R. Deng, P. Y. Zheng, and D. Gall, J. Appl. Phys. **118**, 015706 (2015).
[248] A. Zukauskaite, C. Tholander, F. Tasnadi, B. Alling, J. Palisaitis, J. Lu, Per O. A. Persson, L. Hultmana, and J. Birch, Acta Mater. **94**, 101 (2015).
[249] H. Vollstadt, E. Ito, M. Akaishi, S. Akimoto, and O. Fukunaga, Proc. Jpn. Acad. B **66**, 7 (1990).
[250] A. Mujica, Angel Rubio, A. Muñoz, and R. J. Needs, Rev. Mod. Phys. **75**, 863 (2003).
[251] Q. Xia, H. Xia, and A. L. Ruoff, J. Appl. Phys. **73**, 8198 (1993).
[252] B. Saha, S. Saber, E. A. Stach, E. P. Kvam, and T. D. Sands, Appl. Phys. Lett. **109**, 172102 (2016).
[253] K. N. Tu, IBM J. Res. Dev. **34**, 868 (1990).
[254] M. Zebarjadi, Z. Bian, R. Singh, A. Shakouri, R. Wortman, V. Rawat, and T. Sands, J. Electron. Mater. **38**, 960 (2009).
[255] B. Saha, T. D. Sands, and U. V Waghmare, J. Appl. Phys. **109**, 083717 (2011).
[256] M. Garbrecht, B. Saha, J. L. Schroeder, L. Hultman, and T. D. Sands, Sci. Rep. **7**, 46092 (2017).
[257] G. V. Naik, B. Saha, J. Liu, S. M. Saber, E. A. Stach, J. M. K. Irudayaraj, T. D. Sands, V. M. Shalaev, and A. Boltasseva, Proc. Natl. Acad. Sci. USA **111**, 7546 (2014).
[258] J. L. Schroeder, B. Saha, M. Garbrecht, N. Schell, T. D. Sands, and J. Birch, J. Mater. Sci. **50**, 3200 (2015).
[259] D. Lu, J. J. Kan, E. E. Fullerton, and Z. Liu, Nat. Nanotechnol. **9**, 48 (2014).
[260] C. L. Cortes, W. Newman, S. Molesky, and Z. Jacob, J. Opt. **14**, 063001 (2012).
[261] A. Poddubny, I. Iorsh, P. Belov, and Y. Kivshar, Nat. Photonics **7**, 948 (2013).
[262] G. D. Mahan and L. M. Woods, Phys. Rev. Lett. **80**, 4016 (1998).
[263] D. Vashaee and A. Shakouri, Phys. Rev. Lett. **92**, 106103 (2004).
[264] G. D. Mahan and J. O. Sofo, Proc. Natl. Acad. Sci. USA **93**, 7436 (1996).
[265] A. Shakouri and J. E. Bowers, Appl. Phys. Lett. **71**, 1234 (1997).
[266] B. Saha, A. Shakouri, and T. D. Sands, Appl. Phys. Rev. **5**, 021101 (2018).
[267] J. F. O'Hara, J. M. O. Zide, and A. C. Gossard, App. Phys. Lett. **88**, 251119 (2006).
[268] J. M. O. Zide, A. Kleiman-Shwarsctein, N. C. Strandwitz, J. D. Zimmerman, T. Steenblock-Smith, A. C. Gossard, A. Forman, A. Ivanovskaya, and G. D. Stucky, Appl. Phys. Lett. **88**, 162103 (2006).
[269] H. O. Pierson, *Handbook of Refractory Carbides and Nitrides: Properties, Characteristics, Processing, and Applications* (Noyes Publications, New Jersey, USA, 1996).
[270] M. Murakami, Sci. Techno. Adv. Mater. **3**, 1 (2002).
[271] C. C. Chang, W. J. M. Kort-Kamp, J. Nogan, T. S. Luk, A. K. Azad, A. J. Taylor, D. A. R. Dalvit, M. Sykora, and H.-T. Chen, Nano Lett. **18**, 7665 (2018).
[272] G. V. Naik, J. L. Schroeder, X. Ni, A. V Kildishev, T. D. Sands, and A. Boltasseva, Opt. Mater. Express **2**, 478 (2012).
[273] A. Lalisse, G. Tessier, J. Plain, and G. Baffou, Sci. Rep. **6**, 38647 (2016).